Click Here for Full Article

Variable morphologic expression of volcanic, tectonic, and hydrothermal processes at six hydrothermal vent fields in the Lau back-arc basin

Vicki Lynn Ferrini

Marine Geology and Geophysics Division, Lamont–Doherty Earth Observatory of Columbia University, 61 Route 9W, Palisades, New York 10964, USA (ferrini@ldeo.columbia.edu)

Margaret K. Tivey

Marine Chemistry and Geochemistry Department, Woods Hole Oceanographic Institution, 360 Woods Hole Road, Woods Hole, Massachusetts 02543, USA

Suzanne M. Carbotte

Marine Geology and Geophysics Division, Lamont–Doherty Earth Observatory of Columbia University, 61 Route 9W, Palisades, New York 10964, USA

Fernando Martinez

School of Ocean and Earth Science Technology, University of Hawai'i at Manoa, 1680 East–West Road, Honolulu, Hawaii 96822, USA

Chris Roman

Graduate School of Oceanography, University of Rhode Island, 215 South Ferry Road, Narragansett, Rhode Island 02882, USA

[1] Ultrahigh-resolution bathymetric maps (25 cm grid) are used to quantify the physical dimensions of and spatial relationships between tectonic, volcanic, and hydrothermal features at six hydrothermal vent fields in the Lau back-arc basin. Supplemented with near-bottom photos, and nested within regional DSL-120A side-scan sonar data, these maps provide insight into the nature of hydrothermal systems along the Eastern Lau Spreading Center (ELSC) and Valu Fa Ridge (VFR). Along-axis transitions evident in localized volcanic morphology and tectonic characteristics include a change from broad low-relief volcanic domes (hundreds of meters wide, <10 m tall) that are dominated by pillow and lobate lava morphologies and are cut by faults and fissures to higher aspect ratio volcanic domes (tens of meters wide, tens of meters tall) dominated by aa-type lava morphologies, with finger-like flows, and few tectonic structures. These along-axis differences in localized seafloor morphology suggest differences in hydrothermal circulation pathways within the shallow crust and correlate with regional transitions in a variety of ridge properties, including the large-scale morphology of the ridge axis (shallow axial valley to axial high), seafloor lava compositions, and seismic properties of the upper crust. Differences in morphologic characteristics of individual flows and lava types were also quantified, providing an important first step toward the remote characterization of complex terrains associated with hydrothermal vent fields.

Components: 13,353 words, 14 figures, 1 table.

Keywords: bathymetry; submarine lava morphology; back-arc ridges; Lau Basin.

1. Introduction

[2] Back-arc basin spreading centers exhibit large variations in crustal chemistry, and magmatic and tectonic characteristics, relative to mid-ocean ridges (MORs) [*Pearce et al.*, 1995; *Martinez et al.*, 2006]. The Eastern Lau Spreading Center (ELSC) and Valu Fa Ridge (VFR) are located in the Lau back-arc basin, west of the Tonga Trench between ~19° and 22.2°S (Figure 1). The ELSC was designated as an integrated study site (ISS) of the Ridge2000 (R2K) program to foster coordinated studies of the geological, petrological, geophysical, hydrothermal, and biological characteristics along this western Pacific Ocean back-arc system.

[3] A number of regional differences in geologic setting are evident from north to south along the ELSC and VFR. Spreading rates are fast in the north (97 mm/yr) and slower toward the south (40 mm/yr) with increasing proximity to the subduction zone [*Zellmer and Taylor*, 2001]. Contrary to MOR systems, the ELSC is characterized by a deep flat axial valley in the north where spreading rates are fast, with a transition to a shallow, narrower, peaked axial ridge in the south where spreading rates are slower [*Martinez et al.*, 2006; *Jacobs et al.*, 2007]. This has been attributed to the proximity to and role of the subducting slab in the south affecting mantle chemistry [*Martinez et al.*, 2006]. With decreasing distance between the spreading axis and the arc volcanic front, an increase in magmatic productivity is inferred from bathymetry [*Martinez et al.*, 2006], and an increase in silica content is observed in dredge-recovered lavas [*Pearce et al.*, 1995; *Bezos et al.*, 2005]. Regional surveys of seafloor bathymetry and backscatter intensity have shown a decrease in the extent of faulting and fissuring toward the south [*Martinez et al.*, 2006] that corresponds with a decrease in hydrothermal plume incidence [*Baker et al.*, 2006]. Although a regional decrease in acoustic backscatter intensity toward the south [*Martinez et al.*, 2006] likely implies a relative increase in

sediment cover, it is difficult to infer relative ages from side-scan data because of strong and variable currents that are common along ridge crests and a lack of quantitative information about the relative contribution of hydrothermal sediments.

[4] To further investigate correlations along this back-arc spreading center, particularly relative to hydrothermal activity, six vent fields were investigated during an interdisciplinary research cruise on the R/V *Melville* (TUIM05MV; M. K. Tivey, Chief Scientist) in April/May 2005 (Figure 1). The vent fields are separated from one another by 4 to 140 km, span a total distance of ~245 km, and encompass a large range of regional geologic variability along the ELSC and VFR. Ultrahigh-resolution (submeter) bathymetric data were acquired with a Simrad SM2000 (200 kHz) multibeam sonar system on Remote Operated Vehicle (ROV) *Jason 2*. Multibeam surveys were conducted at 5 to 22 m nominal altitude, and provide sufficient data density and resolution to quantify detailed characteristics of volcanic, tectonic and hydrothermal features. Nested within regional bathymetry [*Zellmer and Taylor*, 2001; *Martinez et al.*, 2006; *Arko et al.*, 2007] and DSL120A (120 kHz) side-scan sonar data [*Martinez et al.*, 2006], and supplemented with ground-truth observations from ROV dives, these ultrahigh-resolution maps provide new insights about the nature and variability of hydrothermal systems in the Lau Basin. They also enable us, for the first time, to quantify morphological characteristics of individual flows and lava types, providing the basic information necessary for building robust remote seafloor characterization tools.

1.1. Identification of Vent Fields at the ELSC/VFR

[5] Studies of active deep sea hydrothermal vent fields rely heavily on the coordinated efforts of researchers investigating different aspects of these complex systems at a range of spatial scales.
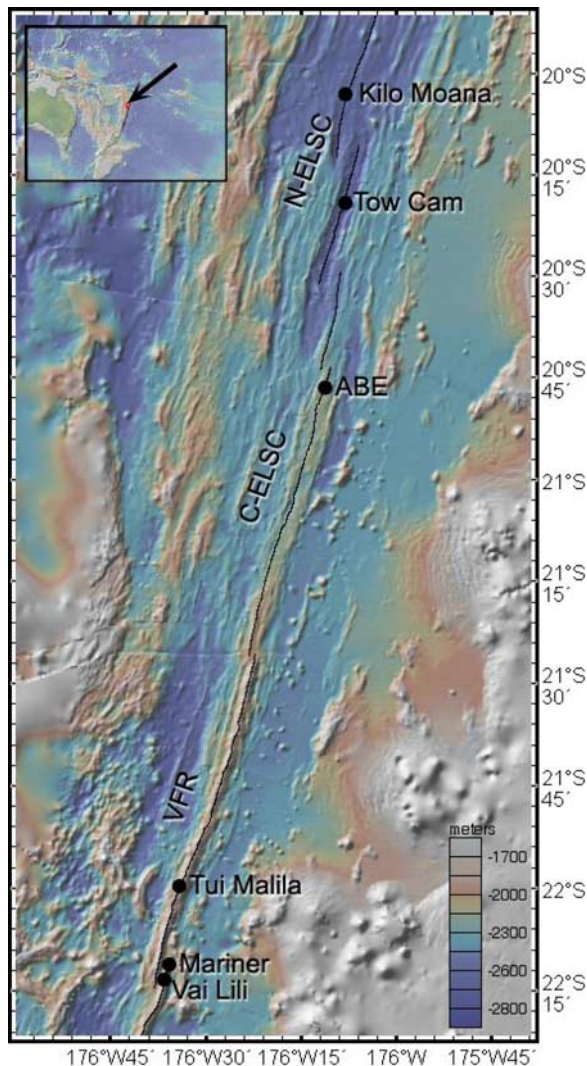
Figure 1. Location of the six vent fields along the ELSC and VFR that were investigated during TUIM05MV. Changes in the characteristics of the spreading center are evident in regional bathymetry [*Zellmer and Taylor*, 2001; *Martinez et al.*, 2006] with a deep, flat spreading center in the north transitioning to a shallow, peaked axis in the south.

Regional bathymetry and side-scan sonar surveys were conducted along the ELSC/VFR with a hull-mounted EM120 multibeam system aboard the R/V *Kilo Moana*, and the towed DSL-120A and IMI30 side-scan sonar systems in April/May 2004 (KM0410; F. Martinez, Chief Scientist) [*Martinez et al.*, 2006]. These surveys include ~400 km of the ELSC/VFR and yielded gridded bathymetric data sets with resolution of 10 to 100 m, and backscatter data gridded at ~5 m. Miniature Autonomous Plume Recorders (MAPRs) were deployed during these geophysical surveys to seek

signals of hydrothermal activity in the water column [*Baker et al.*, 2005, 2006]. Additional water column information was gathered with Conductivity Temperature and Depth (CTD) casts.

[6] A subsequent research cruise (KM0417; C. Langmuir, Chief Scientist) built upon these data sets by deploying the Autonomous Underwater Vehicle (AUV) *ABE* and the WHOI towed camera system *Tow Cam* [*Fornari and the WHOI TowCam Group*, 2003] at locations along the ELSC where plume anomalies [*Baker et al.*, 2006] suggested the presence of hydrothermal activity. *ABE* was used to track water column signals and map the seafloor at 1 to 2 m grid resolution [*Jakuba et al.*, 2005; *German et al.*, 2005; *Yoerger et al.*, 2007]. Near-bottom photos collected with both *ABE* and *Tow Cam* provided ground-truth information that constrained the positions of three active hydrothermal fields (Kilo Moana, Tow Cam, and ABE).

[7] In addition to visiting the vent fields identified along the ELSC during KM0417, two fields (Mariner and Vai Lili) were visited on the VFR. Hydrothermal vents at these locations were first described by French (Vai Lili [*Fouquet et al.*, 1993]) and Japanese (Mariner [*Ishibashi et al.*, 2006]) researchers. The sixth vent field, also on the VFR, was discovered during the TUIM05MV cruise, using CTD and MAPR data from the KM0410 cruise [*Baker et al.*, 2006] to perform additional CTD operations to target the buoyant plume, and identify a dive target for *Jason 2* to investigate its source [*Tivey et al.*, 2005; M. K. Tivey, manuscript in preparation, 2008].

1.2. Near-Bottom High-Resolution Mapping in the Deep Ocean

[8] The resolution of seafloor features in bathymetric maps is fundamentally limited by sonar system parameters (sound frequency, beam spacing and size) which, coupled with survey parameters (survey altitude and speed), define the acoustic footprint size and spatial density of bathymetric soundings on the seafloor. Hull-mounted swath systems operating in 2.5 km water depth can be used to generate bathymetric data sets with resolution of hundreds of meters to tens of meters [e.g., *Macdonald et al.*, 1984, 1992; *Cochran et al.*, 1999; *White et al.*, 2006], while deep-towed side-scan and phase bathymetric swath systems towed closer to the seafloor have been used to create higher-resolution bathymetric maps as good as 5 m resolution [e.g., *Scheirer et al.*, 2000; *Martinez et al.*, 2006].

[9] Advances in both sonar technology and precision underwater vehicle navigation now permit well-navigated near-bottom mapping of deep sea features at meter scale or better [e.g., *Yoerger et al.*, 1996; *Ballard et al.*, 2000; *Ferrini et al.*, 2007]. Such high-resolution bathymetric maps have been generated at a number of deep sea sites with high-frequency sonar data collected with deep submergence ROVs [*Ballard et al.*, 2000; *Whitcomb et al.*, 2000; *Singh et al.*, 2000; *Roman*, 2005], AUVs [e.g., *Yoerger et al.*, 1996; *Schouten et al.*, 2002; *Shank et al.*, 2003; *Caress et al.*, 2006], and Human Occupied Vehicles (HOVs) [*Kurras et al.*, 1998; *Chadwick et al.*, 2001; *Soule et al.*, 2005; *Escartin et al.*, 2007; *Ferrini et al.*, 2007]. With these kinds of near-bottom surveys, the precision of underwater vehicle navigation imposes more of a limitation on the resolution of data products than sonar parameters [*Singh et al.*, 2000; *Roman and Singh*, 2007]. Positional offsets on the order of meters are not uncommon with underwater navigation techniques and can compromise the quality of bathymetric data products [*Ferrini et al.*, 2007]. Additional processing steps are therefore required to ensure the proper geospatial registration of seafloor features to enable the creation of ultrahigh-resolution (submeter) bathymetric data products [*Ferrini et al.*, 2007; *Roman and Singh*, 2007].

[10] Ultrahigh-resolution bathymetric maps of deep sea hydrothermal vent fields not only provide base maps for interdisciplinary studies, but can be used to quantify the morphologic characteristics and spatial relationships between tectonic, volcanic and hydrothermal features [*Soule et al.*, 2005; *Escartin et al.*, 2007; *Ferrini et al.*, 2007]. With repeat surveys, these data can be used to quantify bathymetric change over a range of spatial and temporal scales to better understand the physical processes that shape the seafloor (V. L. Ferrini, manuscript in preparation, 2008). High-quality ultrahigh-resolution bathymetric maps also provide the basis for developing quantitative seafloor characterization tools to aid in the geologic interpretation of the seafloor.

2. Methods

2.1. Data Acquisition

[11] Near-bottom bathymetric data were acquired with a Simrad SM2000 200 kHz multibeam sonar system mounted on ROV *Jason 2*. *Jason 2* is equipped with a high-precision navigation system consisting of a bottom-lock acoustic Doppler Velocity Log (DVL) dead-reckoning navigational system that is constrained by Long BaseLine (LBL) acoustic navigation and supplemented with a gyrocompass. The SM2000 multibeam system has an angular sector of 120°, with even beam spacing of 0.94°, and a beam width of 1.5°. It can be operated at ranges of 5 to 400 m and has a range resolution of 2 cm, with ping rates as high as 20 Hz.

[12] Bathymetric data were collected during dedicated sonar surveys and near-bottom photographic surveys while conducting an interdisciplinary sampling program at six vent fields along the ELSC and VFR (Figure 1). Survey speed was 0.25 m/sec and altitudes ranged from 5 to 22 m depending on the operational goals of each dive. No bathymetric data were acquired at survey altitudes less than the minimum range required for the SM2000 (5 m). Survey lines were spaced assuming a 90° sector (swath width: 2 times altitude) to minimize reliance on data collected with the outer beams. Survey line spacing was generally 1 times altitude which yielded 100% overlap between adjacent lines and resulted in dense data coverage.

2.2. Data Processing

[13] Navigational data were processed using a suite of MATLAB programs to clean the LBL data and merge it with the DVL data [*Kinsey et al.*, 2006; *Ferrini et al.*, 2007]. Simultaneous Localization And Mapping (SLAM) methodology [*Roman*, 2005; *Roman and Singh*, 2007] was then employed to register overlapping submaps (small regions of consecutive pings) of the bathymetric data set. The SLAM algorithm utilized real-time DVL velocity data and was geospatially constrained with the postprocessed LBL position data. The resulting bathymetric soundings were manually edited using the Fledermaus™ 3D Editing tool to provide a final level of quality control.

[14] At 20-m altitude, the estimated acoustic footprint size ranges from ~0.27 m^2 near nadir to 1.09 m^2 at a 45° angle of incidence, while at 5-m altitude, the footprint is ~0.01 m^2 near nadir and 0.07 m^2 at 45° (Figure 2). Given the data density that resulted from closely spaced lines, and the fact that some surveys (and/or portions of surveys) were conducted at altitudes less than 20 m, the bathymetric data were gridded at 25 cm resolution. Typical data density ranged from 130 soundings per grid cell during surveys conducted at 5-m altitude, to ~40 soundings per grid cell during
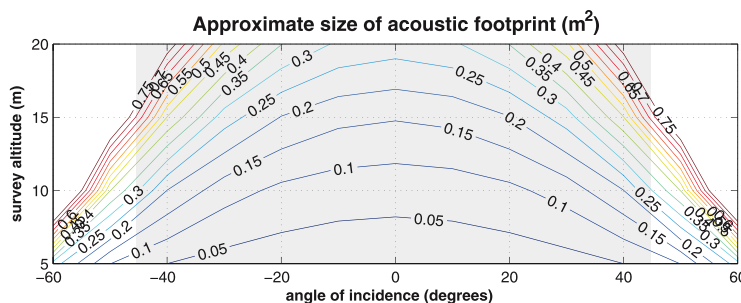
Figure 2. Estimated size of acoustic footprint at different altitudes and angle of incidence, assuming a flat seafloor. Gray area indicates the range of survey altitudes and angles of incidence that pertain to the near-bottom SM2000 data collected with ROV *Jason 2* at the ELSC/VFR. Since the survey lines were closely spaced, data with large acoustic footprints (large angle of incidence) are complemented with data with small acoustic footprints (small angle of incidence) acquired along adjacent survey lines.

higher altitude surveys. Although some data that were acquired at lower survey altitudes were gridded at 15 cm resolution, final data products are provided at 25 cm resolution to maintain consistency throughout the bathymetric maps generated for all six vent fields. Data were gridded using a weighted mean interpolation method with a Gaussian basis function (search radius: 1 m, sigma value: 0.5 m). Bathymetric grids and 3-D visualizations, ASCII data files with bathymetric soundings, and navigational data files are available through the Ridge2000 Data Portal of the Marine Geoscience Data System (http://www.marine-geo.org/link/entry.php?id=TUIM05MV) [*Carbotte et al.*, 2004].

2.3. Nested Data Sets and Ground-Truth Imagery

[15] Ultrahigh-resolution SM2000 bathymetry grids were nested within regional bathymetric data accessed through the data visualization and analysis tool GeoMapApp (http://www.geomapapp.org) to understand the regional tectonic setting of each vent field. Existing multibeam bathymetry [*Zellmer and Taylor*, 2001; *Martinez et al.*, 2006] and side-scan data [*Martinez et al.*, 2006] available through the Ridge 2000 Data Portal (http://www.marine-geo.org/ridge2000) [*Carbotte et al.*, 2004] were used to characterize regional volcanic and tectonic features proximal to each vent field.

[16] Morphologic features identified in ultrahigh-resolution bathymetry data were ground-truthed with still images captured with *Jason 2* (Figure 3) during our cruise and two subsequent cruises to the Lau ISS (TUIM07MV and MGLN07MV, C. Fisher Chief Scientist). These images are available through the National Deep Submergence Facility (http://

www.whoi.edu/page.do?pid=8475), and are also accessible in map view through GeoMapApp. Relative chronology of volcanic and tectonic activity is inferred on the basis of the relationships between morphologic features identified in the ultrahigh-resolution maps and observations of sediment cover from ground-truth imagery.

2.4. Roughness Analysis

[17] As a first step toward quantitative seafloor characterization with ultrahigh-resolution bathymetric maps, rugosity was used as a measure of seafloor roughness. Rugosity, the ratio of true surface area to planar surface area, was computed using a Delaunay triangulation of gridded data points (25 cm grids) for 20 × 20 m regions of known morphology within each bathymetric map. Unlike grid-based rugosity algorithms used by others [*Jenness*, 2003, 2004; *Lundblad et al.*, 2006], our rugosity algorithm uses the MATLAB Delaunay triangulation function to create a Triangulated Irregular Network (TIN) surface from the gridded bathymetry values. Rugosity is then calculated for each triangle in the TIN by taking the ratio of the true (3-D) surface area to the planar (2-D) surface area. Rugosity values for each triangle are then gridded at the same resolution as the input grid to generate a rugosity grid. Direct comparisons of the results of our TIN-based rugosity algorithm with grid-based rugosity values [*Jenness*, 2004], indicate that they are highly correlated (Spearman coefficient: 0.98).

[18] Rugosity grids are frequently used as derivative layers in Geographic Information System (GIS) classification schemes [e.g., *Lundblad et al.*, 2006], but we instead characterize their frequency distribution to quantify differences in sea-
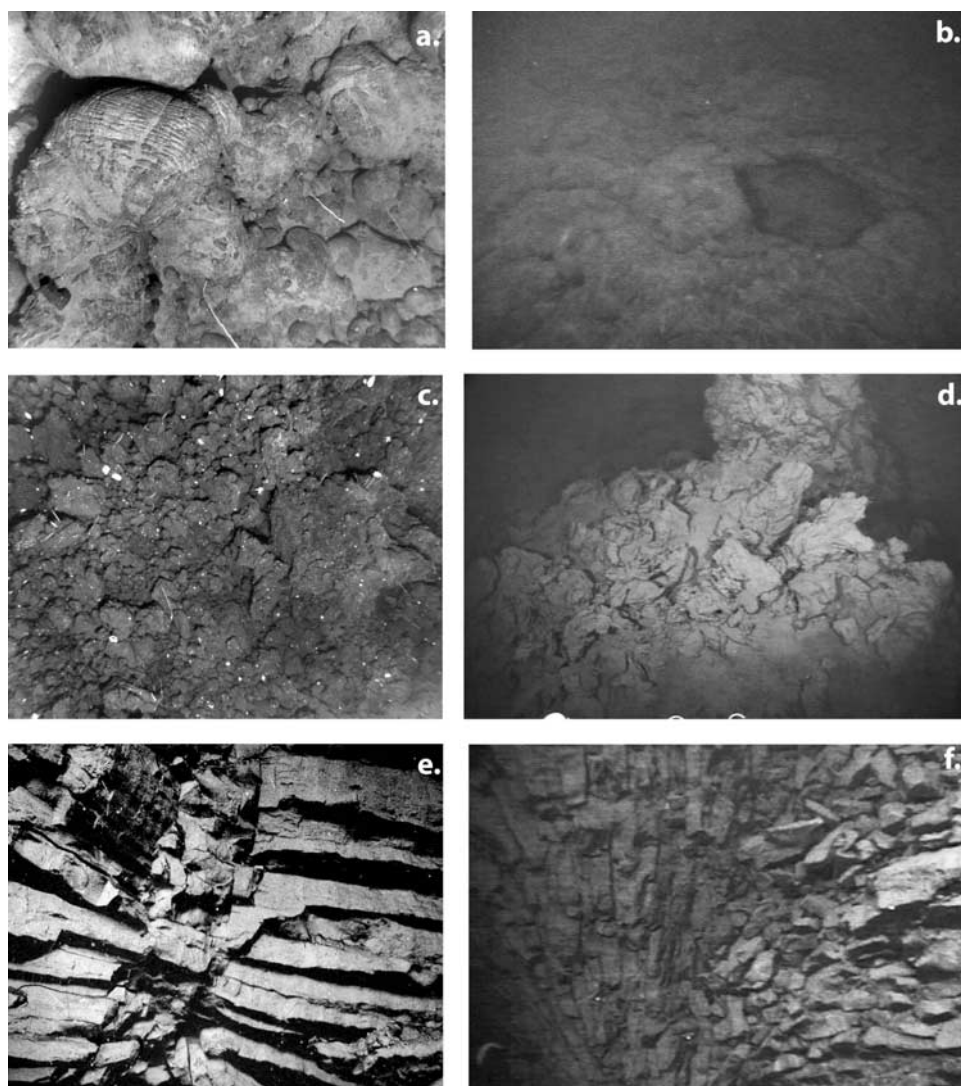
Figure 3. Example images acquired with ROV *Jason 2* that were used to ground-truth ultrahigh-resolution bathymetry maps. (a) Top view of pillow lavas that characterize the Kilo Moana vent field. On the basis of the vehicle altitude this image is approximately 1.6 m across. (b) Oblique view of collapsed lobates observed at the Tow Cam vent field. (c) Top view of aa-type flow observed at the Tui Malila vent field. On the basis of vehicle altitude, the image is approximately 1.5 m across. (d) Oblique view of aa-type flow observed at the Mariner vent field. (e) Forward looking view of columnar jointing observed along a fault scarp at Tui Malila. Individual columns in this picture are approximately 20 cm thick. (f) Forward looking view of columnar jointing observed at the ABE vent field.

floor roughness based on areas of known seafloor morphology. Graphic (percentile) statistics, similar to those used for grain size distribution [*Folk and Ward*, 1957], were used to quantify the frequency distributions for several rugosity grids from each vent field. Quantitative differences in morphology type (e.g., pillow lavas versus sedimented areas, faults/fissures and flow fronts) and along-axis variability in roughness characteristics were assessed by comparing the graphic statistics (mean, median, standard deviation, kurtosis, skewness) derived from cumulative percentage curves of rugosity. Rugosity grids were also computed from

ultrahigh-resolution bathymetry data from the East Pacific Rise (V. L. Ferrini, manuscript in preparation, 2008; S. A. Soule et al., submitted manuscript, 2008) to help constrain the potential effects of substrate composition on rugosity characteristics.

3. Results 1: Vent Field Descriptions

3.1. Kilo Moana

[19] The Kilo Moana vent field is located along the Northern ELSC (N-ELSC), at 176°08.03′W, 20°03.15′S, 2620 m water depth (Figure 4). Hosted

in basaltic substrate [*Bezos et al.*, 2005; *Ridge* 2000, 2006], it is located 17 km north of the southern end of a 100 km long segment, and was first identified as an active hydrothermal field during KM0417 (Langmuir). At Kilo Moana axial relief is subdued and the innermost axis coincides with a narrow depression <1 km wide and <100 m deep (Figure 4). South of Kilo Moana the ridge axis curves into an overlapping configuration with the adjacent segment to the south. Seamounts flanking the spreading center and bathymetric characteristics of the overlapping spreading center region contribute to a poorly defined axial valley (Figure 4a). The Kilo Moana vent field sits ap-

proximately 500 m west of the inferred spreading axis on a short (15 m), wide (2 km) and slightly asymmetric bathymetric high that is steeper on its western side (Figure 4b).

[20] The ultrahigh-resolution bathymetry map of Kilo Moana reveals what appears to be two broad (~120 m) low relief (<6 m) volcanic domes that are crosscut by two well-defined fissures (Figure 5). The western fissure is at least 9 m deep, with variable width of 4–20 m, while the eastern fissure is narrower and deeper, with a maximum depth of at least 10 m, and a width of ~5 m. A remnant down-dropped block in the middle of the western fissure lies ~4 m below the bounding fissure walls. Hydrothermal vent structures are clearly evident in the bathymetric data, and are located adjacent to and at the intersection of the two fissures. The seafloor is otherwise relatively flat with a bumpy texture with amplitudes of 0.1 to 0.4 m over distances of 0.5 to 1 m (Figure 5a), which ground-truth observations indicate is associated with pillow lavas (Figure 3a).

[21] Confirmed hydrothermal activity at Kilo Moana (from ROV visual observations) extends N–S over a distance of approximately 130 m, with three localized areas of focused high-temperature venting and diffuse flow separated by the two fissures [*Tivey et al.*, 2005] (Figure 5). In the northernmost area of venting, diffuse flow was observed both within the fissure and on its western wall, and two bulbous high temperature chimney edifices (one that is 4 to 5 m in diameter and >5 m tall) were identified on the western wall. The central area of venting at Kilo Moana is located between the two large fissures, ~50 m south of the
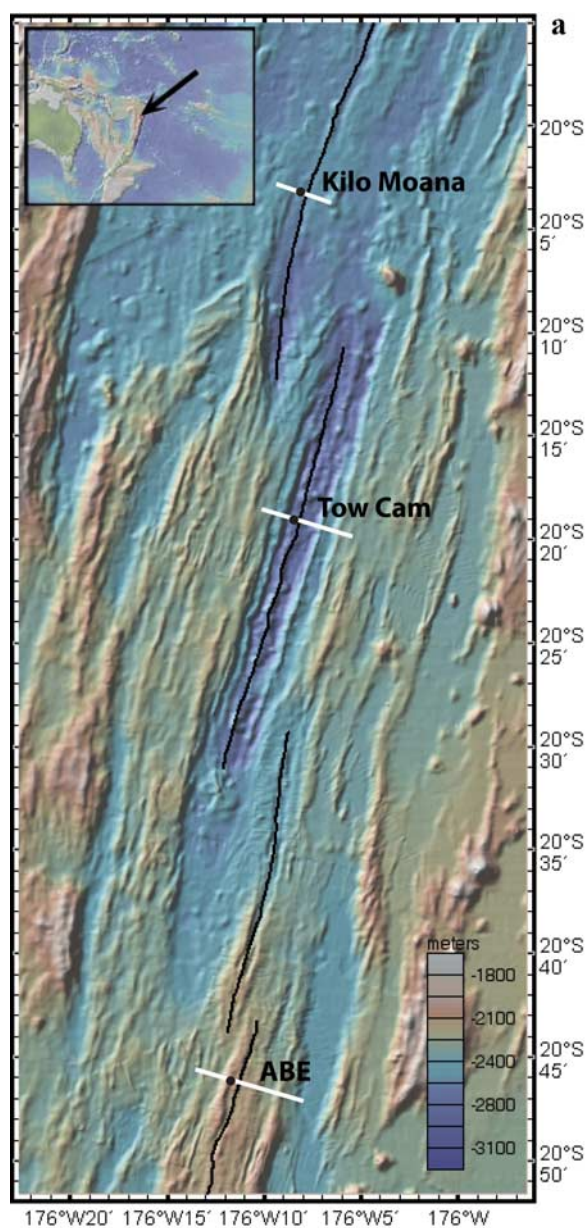

Figure 4. (a) Regional bathymetry of the N-ELSC and C-ELSC, which host the Kilo Moana, Tow Cam, and ABE vent fields. Note the regional transition in axial morphology with a flat poorly defined spreading center at Kilo Moana transitioning to a well-defined axial valley at Tow Cam, and an axial ridge at ABE. The inferred location of the spreading axis [*Martinez et al.*, 2006] is indicated with a black line, and black dots indicate the location of each vent field. (b) Bathymetric profile across the Kilo Moana vent field, the location of which is identified with a white line in Figure 4a. The axis at this location is poorly defined, and the innermost axis coincides with a narrow depression <1 km wide and <100 m deep. (c) Bathymetric profile across the Tow Cam vent field reveals a well-defined axial valley (2.5 km wide, 300 m deep) in which the vent field is offset to the west of the spreading axis. (d) Bathymetric profile across the ABE vent field, which is located on an axial ridge (4.2 km wide, ~200 m tall). The vent field is situated approximately 600 m west of the spreading axis within a rift.
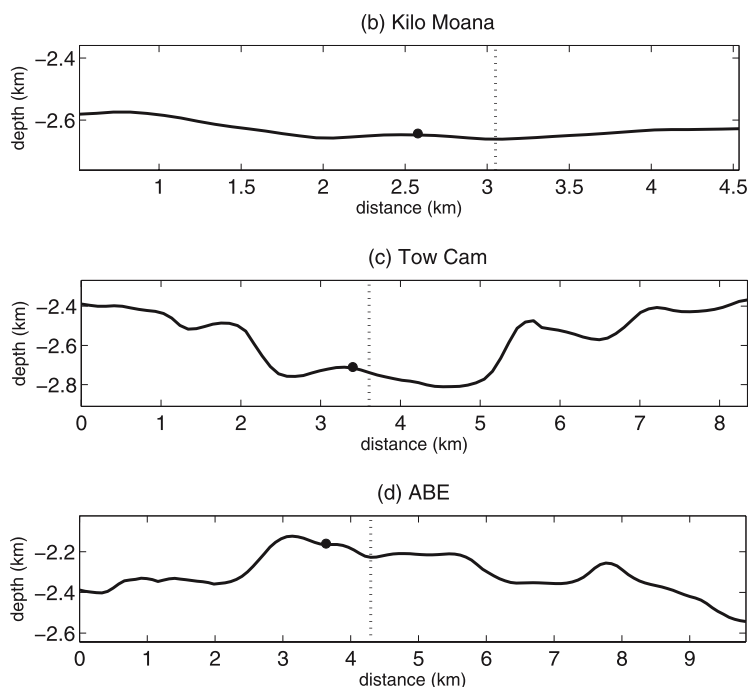
Figure 4. (continued)

northern vents on relatively flat seafloor composed of pillows, and consists of two vent edifices (~7 and 16 m tall, both ~3 m in diameter) and an area of diffuse flow (Figure 5). Some inactive and active individual chimneys are present at the bases of these edifices. These edifices appear as pinnacles in the map, but visual observations from the ROV indicate that they are edifices of coalesced pipes, some with cactus-like protrusions that extend out 0.5 m and then rise upward [*Tivey et al.*, 2005]. Differences in observed vent morphology and 3-D visualizations are the result of gridding the bathymetric data points into a single surface causing vent structures to appear conical. Two localized areas of activity are present in the south at Kilo Moana, both east of the eastern fissure. Diffuse flow and at least 4 vent edifices were observed along the edge of the fissure (Figure 5). To the north–northeast, at least two ~5 m tall, ~3 m diameter edifices are present (Figure 5). Ground-truth observations indicate that these edifices consist of coalesced pipes, some with cactus-like protrusions [*Tivey et al.*, 2005], and that the substrate within the vent field is dominated by pillows with little sediment cover (Figure 3a).

[22] The regional DSL-120A side-scan data (Figure 5b) reveal that the area surrounding Kilo Moana is dominated by faults and fissures, and the fissures that cut through the vent field extend for over 1 km N–S. A third fissure ~600 m long is located 80–100 m east of the eastern fissure that cuts through the vent field. The DSL-120A data also reveal nearby (<1 km) volcanic domes cut by faults and fissures that are similar to those within the vent field, as well as apparent cracked inflation domes (~100 m diameter). Although locally dominated by fissures, regional EM120 and DSL120A data indicate that the segment of the N-ELSC that hosts Kilo Moana is characterized by fewer tectonic features than the adjacent segments to the north and south [*Martinez et al.*, 2006].

3.2. Tow Cam

[23] The Tow Cam vent field is located along the ridge segment immediately to the south of the Kilo Moana vent field at 176°08.2′W, 20°19.0′S, 2700 m water depth (Figure 4). It lies 16 km south of the end of a 39 km linear ridge segment, within a well-defined axial valley ranging from 270 to 330 m deep with a width of 2.5 km (Figure 4c). The vent field is located atop an elevated asymmetric ridge that is offset west of the center of the axial valley, and is 75 m tall and ~1.8 km wide.

[24] The ultrahigh-resolution map of Tow Cam reveals a normal fault with 10–20 m throw along the western margin of the survey area (Figure 6). A smaller subparallel fault (throw ~1.2–1.5 m) located 30–50 m to the east connects two localized areas of
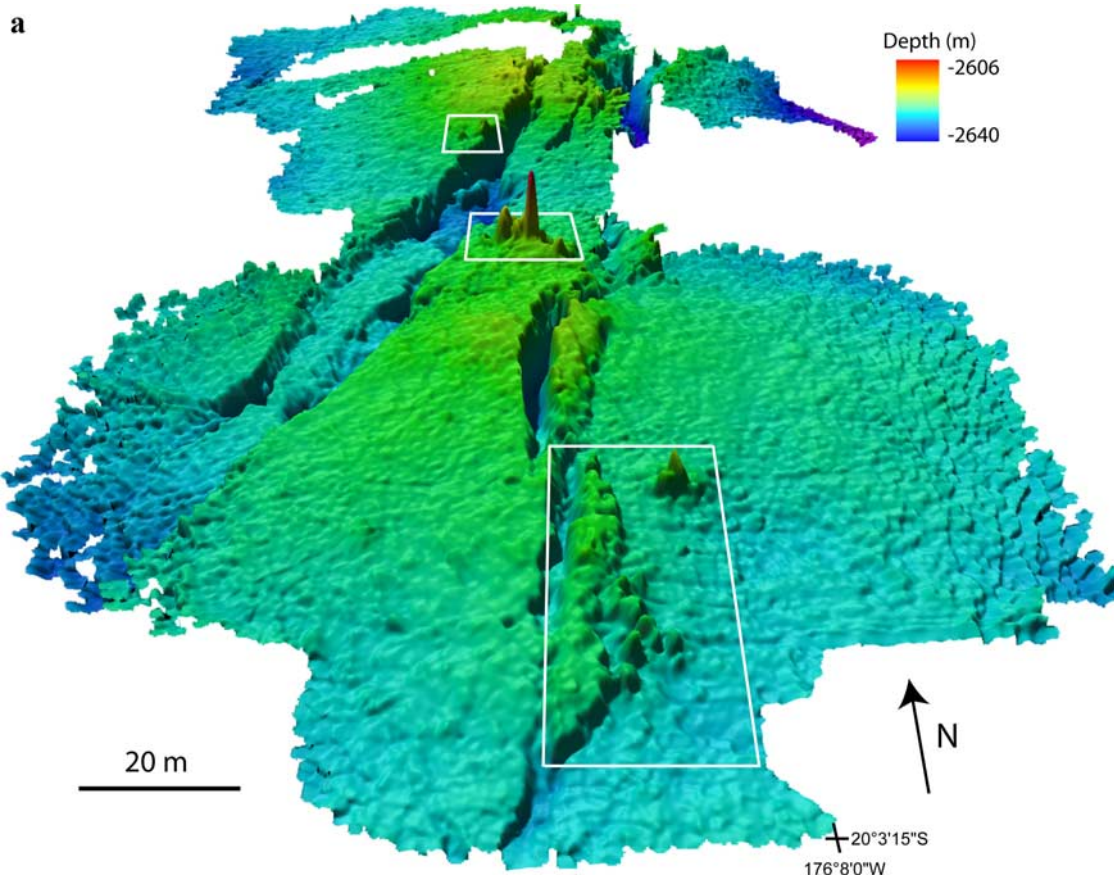
Figure 5. (a) Kilo Moana vent field on the N-ELSC. Perspective view of ultrahigh-resolution (25 cm) SM2000 bathymetric map of the Kilo Moana vent field reveals a bumpy texture related to pillow lavas. Areas of observed hydrothermal activity (both focused and diffuse flow) are outlined with white boxes. Tall, straight-sided to bulbous vent edifices up to 19 m tall are evident between the two fissures that crosscut the vent field, but appear conical in this visualization because of the nature of the gridding algorithm. (b) Geologic interpretation of vent field based on ultrahigh-resolution bathymetry, ground-truth images, and regional context provided by DSL120A side-scan data [*Martinez et al.*, 2006]. Areas of low backscatter intensity are dark, and areas of high backscatter intensity are light.

actively venting hydrothermal deposits separated by ~195 m. A shallow dome (~180 m diameter, ~20 m height) similar to those observed in the Kilo Moana region is cut by both faults and separates the two clusters of vent structures (Figure 6b). With the exception of the faults, the gradually sloping seafloor is characterized by a bumpy texture similar to that observed at Kilo Moana (0.1 to 0.5 m relief, 0.5 to 1 m width, Figure 6a), which ground-truth observations confirm to be pillow/lobate terrain.

[25] Ground-truth observations also reveal differences in vent activity in the northern and southern areas. Like at Kilo Moana, little sediment cover was observed on the surrounding pillow/lobate substrate. The northern vent area is on the northern edge of the dome and consists of at least 4 discrete vent edifices (3–15 m tall and ~2 to 3 m in

diameter) that extend ~30 m E–W. By contrast, the southern area consists of several smaller active and inactive chimneys (<1 to 5 m tall) that are associated with diffuse flow. An ~8 m diameter mound capped with small pipe-like active chimneys is present in the northeast part of the southern area, and further south there are two taller and broader vent edifices. Areas of diffuse flow with maximum observed temperatures of 24°C were also observed within the Tow Cam vent field on the slopes of the broad dome and surrounding some of the southern active chimneys (Figure 5d). Ground-truth observations reveal localized areas of collapsed lobate flow on the top of the broad dome that dominates the vent field (Figures 3a and 6b).

[26] DSL120-A data reveal that the larger fault along the western edge of the Tow Cam vent field
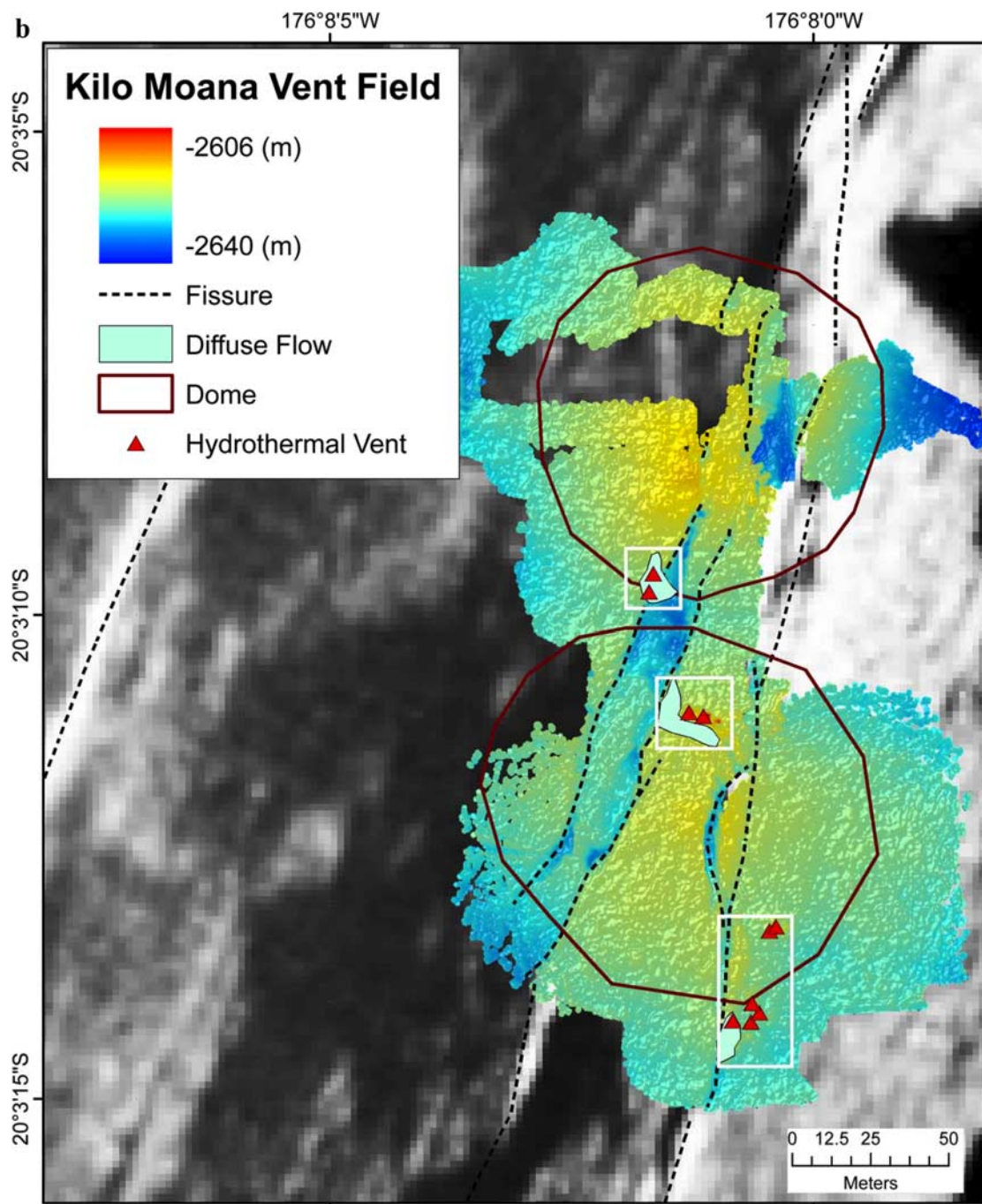
Figure 5.   (continued)

is continuous for many kilometers to the north and south. It steps eastward by ~200 m approximately 500 m north of the vent field, and its throw increases to the south, apparently doubling approximately 800 m south of the vent field. A series of fissures are evident approximately 1 km to the NE of the vent field, and numerous broad domes

(diameters: 100–200 m) are evident within 500 m of the vent field.

3.3. ABE

[27]   The ABE vent field, along the central segment of the ELSC (C-ELSC) at 176°11.5′W, 20°45.8′S, 2140 m water depth, is located at the northern end
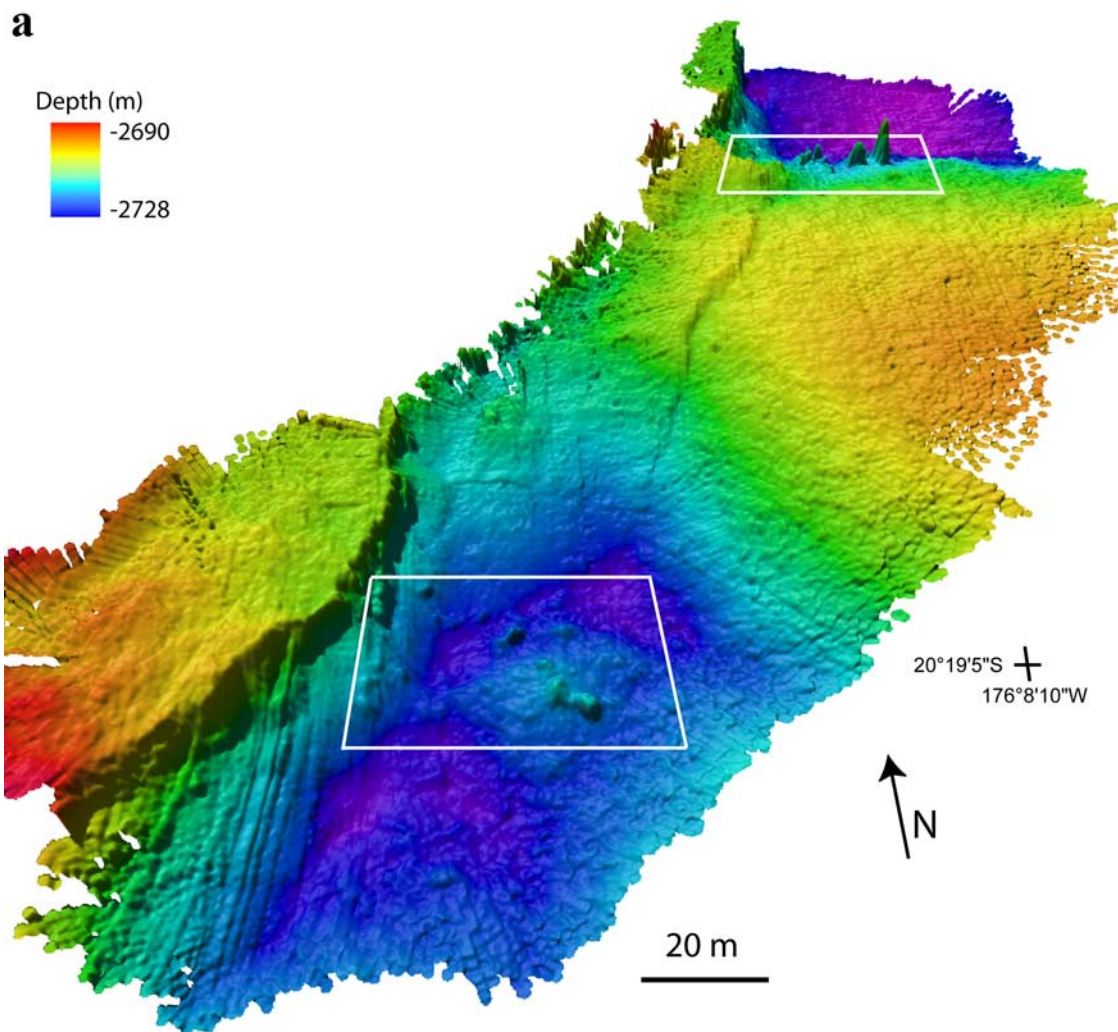
Figure 6. (a) Tow Cam vent field on the N-ELSC. Perspective view of ultrahigh-resolution bathymetric map revealing a bumpy texture related to pillow and lobate lavas. Note that vent edifices within two areas of focused hydrothermal activity (outlined with white boxes) are clearly identifiable in the bathymetry data and are located adjacent to a normal fault with <20 m throw. These hydrothermal vent areas are directly connected by a small fault (throw ∼ 1 m). Small N−S trending linear steps near the fault scarp in the southern extent of the survey area are due to sonar artifacts. (b) Geologic interpretation of the Tow Cam vent field overlain on the bathymetry data and nested within the DSL120A side-scan data [*Martinez et al.*, 2006]. Two broad areas of diffuse flow are also identified. Areas of low backscatter intensity are dark, and areas of high backscatter intensity are light. Ticks on fault lines are on the downthrown blocks.

of an 80 km ridge segment, 5 km south of a 2.5 km left stepping offset (Figure 4). This portion of the ridge is broad (4.2 km) and tall (∼200 m), and the vent field is situated approximately 600 m west of the spreading axis, east of a normal fault with ∼30 m throw (Figure 4d).

[28] A NE−SW trending fault dominates the survey area, with a throw of 10−20 m (Figure 7). The fault has several parallel steps and, in some places, a scalloped character. A second, parallel fault (10−12 m throw) is evident along the western edge of the survey area, approximately 145 m west of the main fault. A third, smaller fault (∼8 m throw) is evident at the NE edge of the survey area (Figure 7c).

[29] Several distinct surface morphologies are evident throughout the ABE survey area, and at least three lava flow fronts are identifiable (Figure 7c). A flow emanating from the west is evident on the fault block in the NW corner of the survey area. Ground-truth observations indicate that this region
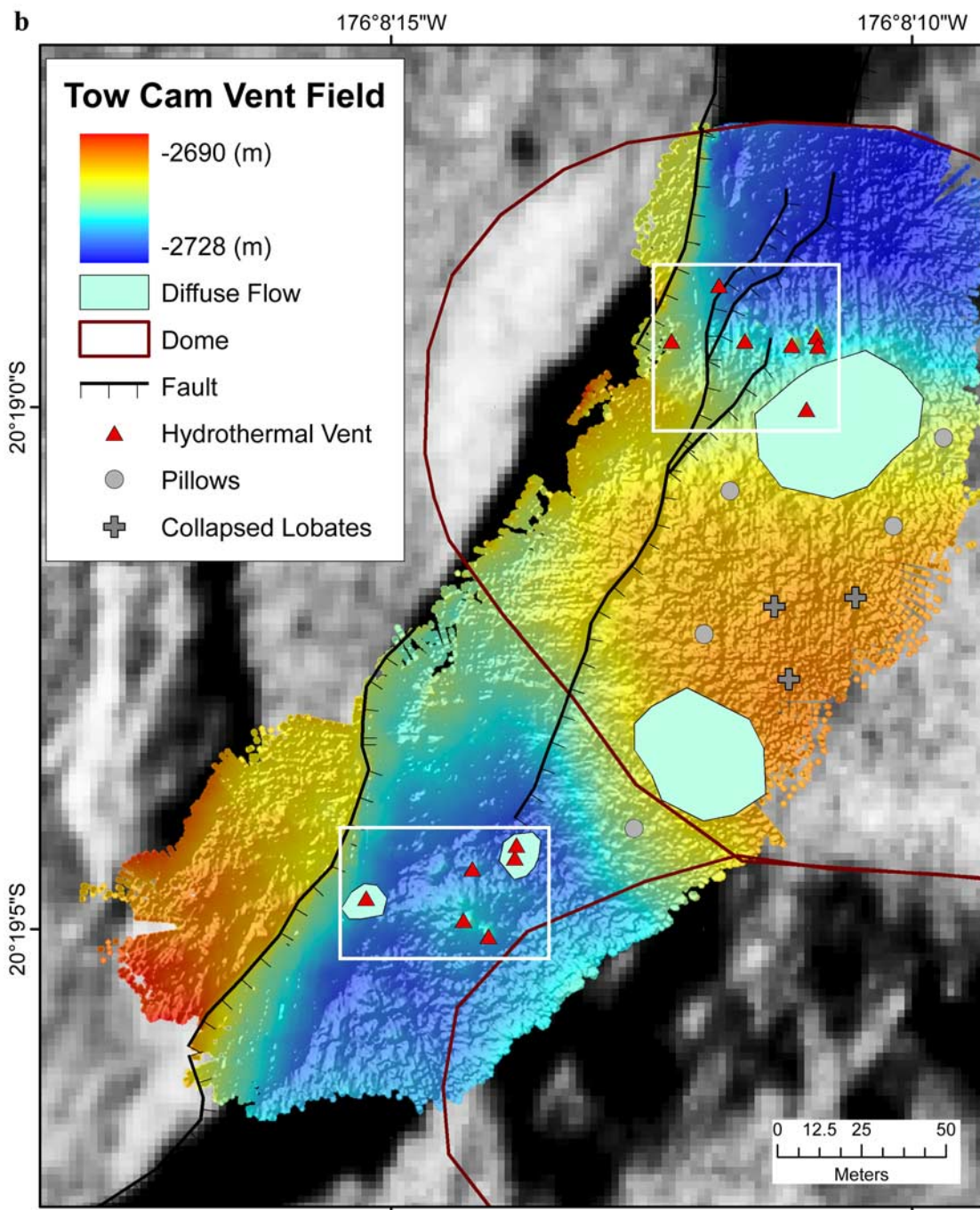
Figure 6. (continued)

is heavily sedimented. East of the fault scarp in the NE corner of the survey area, finger-like flow fronts (individual fingers 3 to 4 m tall and 4 to 5 m wide) emanate from the east and have a smooth, sometimes striated, surface with no sediment cover (Figure 7d). A third flow composed of pillow/lobate lava, apparently emanating from the east, is evident between the central and southern vent areas (Figure 7c). South of the southern vent area, another pillow/lobate flow front is evident emanating from the east. Owing to limited data coverage, it is unclear from the bathymetry data whether this flow is distinct from the other pillow/lobate flow. Localized areas with bumpy texture similar to that seen at Kilo Moana and Tow Cam
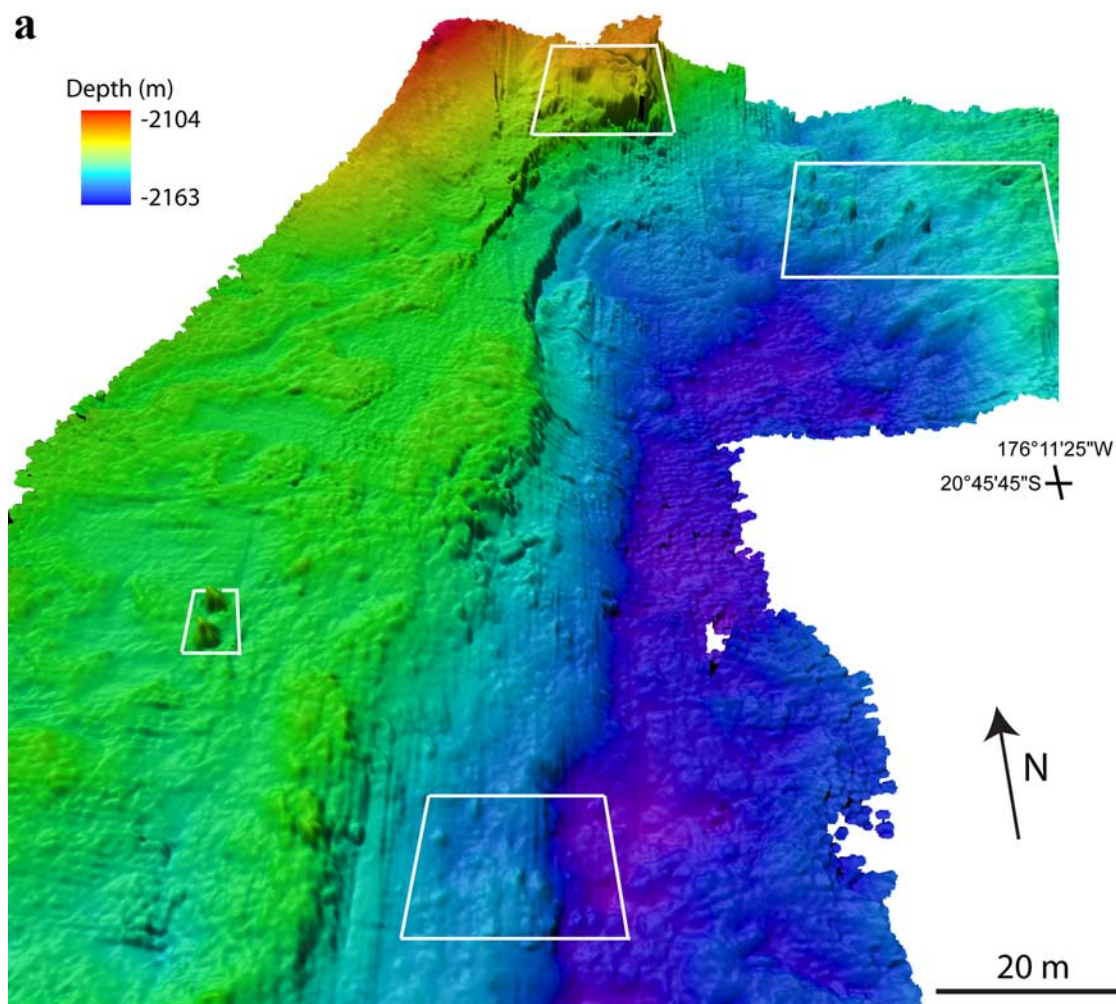
Figure 7. (a) ABE vent field on the C-ELSC. Perspective view of northern and central areas of hydrothermal venting located on the fault scarp and adjacent to it. Observed areas of hydrothermal activity (both focused and diffuse flow) are outlined with white boxes. Individual vent edifices are identifiable in this view, and finger-like flows are evident within the white box at the northeastern extent of the view. (b) Perspective view of southern area of hydrothermal activity which is on a platform between the two faults. (c) Geologic interpretation of ultrahigh-resolution bathymetry nested within DSL-120A side-scan data [*Martinez et al.*, 2006]. All areas of diffuse and focused hydrothermal activity identified in Figures 7a and 7b are outlined with white boxes. Areas of low backscatter intensity are dark, and areas of high backscatter intensity are light. Numerous flow fronts are identifiable in the ultrahigh-resolution bathymetry, most of which were sourced from the east. Columnar jointing was observed in two locations along the fault scarp. (d) Image of tabular lava in the northwest extent of the survey area that is associated with finger-like flows.

are also evident throughout the ABE survey area (Figures 7a and 7b).

[30] Hydrothermal activity was identified during ROV operations at three areas along 600 m of the NE–SW trending fault that dominates the site (Figure 7). The northern region of hydrothermal activity extends nearly 100 m in the NW–SE direction, oblique to the fault. Visual observations confirm that the eastern extent of this region of activity consists of hydrothermal vent edifices that

are branched and include flanges [*Tivey et al.*, 2005], while the western extent of activity consists of diffuse flow located on the fault scarp (Figures 7a and 7c). Ultrahigh-resolution bathymetry indicates that some vent edifices and flanges are superimposed on the finger-like flows emanating from the NE. Near-bottom photos of the substrate near these vent edifices reveal a domed sheet-like substrate that is striated and cracked and has no sediment cover (Figure 7d). Nearby vent edifices, located a few
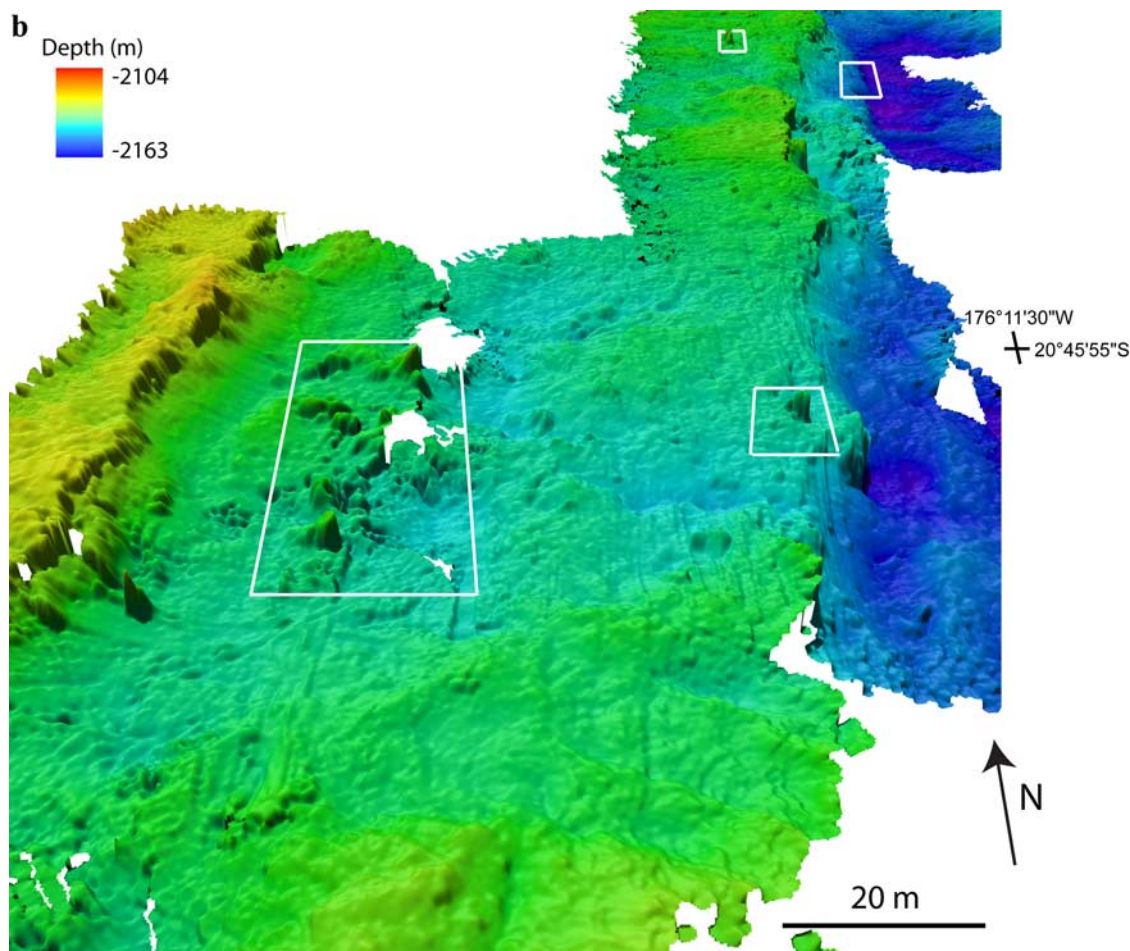
Figure 7.   (continued)

meters to the NW, are hosted on aa-type lava flows (Figure 3c).

[31] Two central area of hydrothermal activity are present at ABE, one east of the dominant fault scarp (throw: 20 m total, but broken into 2 steps each with ~10 m throw) and ~250 m south of the northern vents (Figure 7), and another to the west on top of the scarp. At the eastern area, numerous small narrow venting spires (<1 m tall) are surrounded by diffuse flow and located along and adjacent to the stepped fault scarp. Some spires are evident as small bathymetric features (<0.5 m tall) but most are obscured by the variable bathymetry associated with the fault scarp. Hydrothermal activity at this location extends tens of meters E–W, orthogonal to the N–S trend of the fault scarps. On the top of the scarp, are two ~3 m diameter tall complexes of coalesced pipes; the edifices are narrower at the base and branch outward, with active small chimneys present at the top of the edifices.

[32] The southern hydrothermally active region (~300 m further south) consists of two areas of localized activity approximately 85 m apart, both characterized by 3 to 8 m tall hydrothermal vent edifices. Situated on the platform between the two faults, the easternmost vents are near the top edge of the eastern fault block (12 to 20 m throw), and the western vents are near the base of the western fault scarp.

[33] Ground-truth observations reveal columnar jointing exposed along the fault scarp, between the northern and central vent areas, and between the central and southern vent area (Figures 7c and 3f). Heavy sedimentation was observed on the tops of the fault blocks in the extreme northern and southern extent of the survey area associated with smooth seafloor in ultrahigh-resolution bathymetry maps. Moderate sediment cover was observed between the central and southern vent areas.

[34] The DSL-120A side-scan data indicate that the faults that cut through the ABE vent field merge
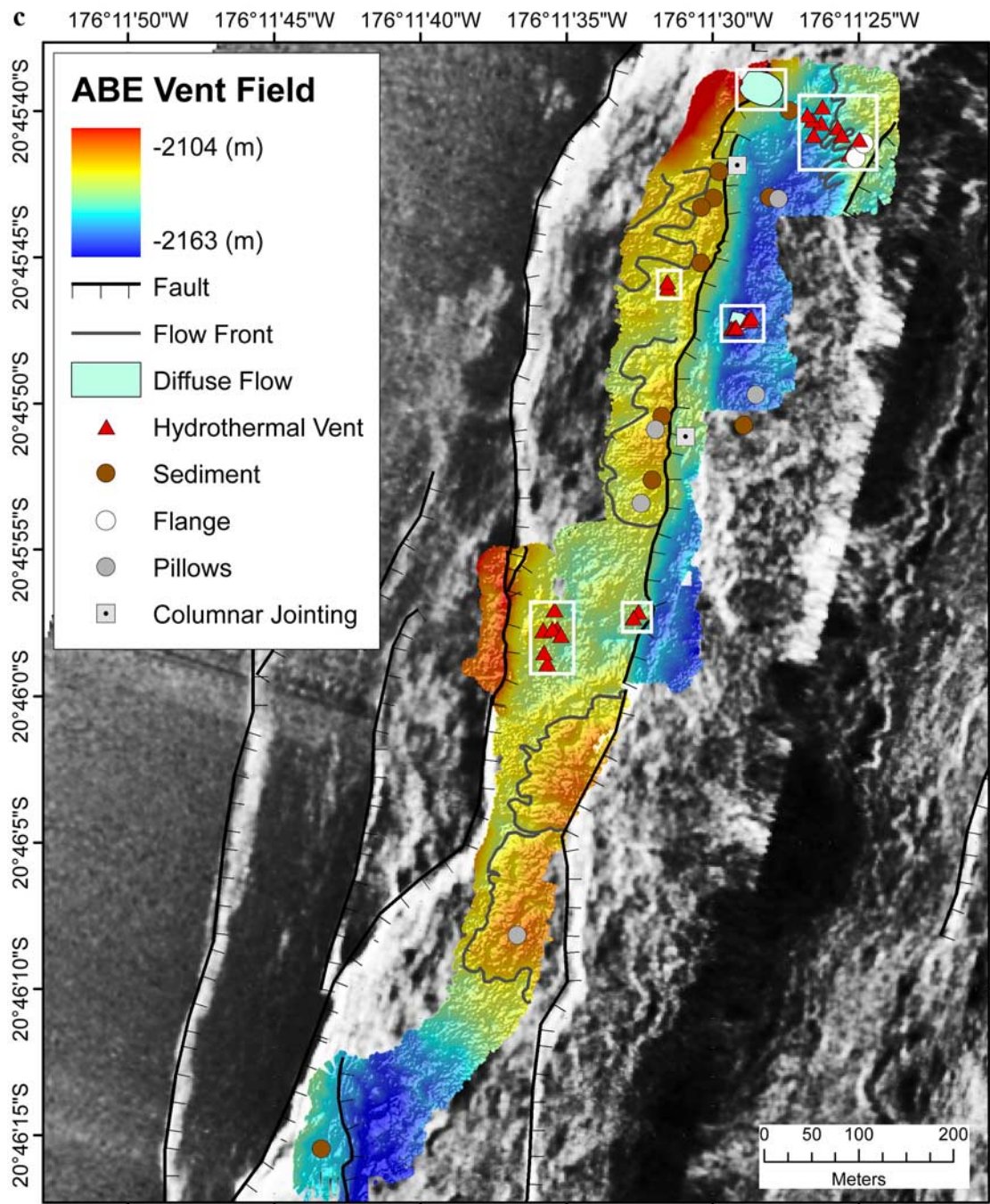
Figure 7. (continued)

both north and south of the surveyed area and extend for approximately 6 km. Many additional faults with lengths of 1 km or more are evident in the region surrounding the vent field. Several small dome-like structures (~100 m diameter) are evident south and east of the vent field in the DSL-120A side-scan data.

3.4. Tui Malila

[35] The Tui Malila vent field is located on the VFR at 176°34.06′W, 21°59.35′S, 1870 m water depth (Figure 8a). The spreading center here is characterized by a ridge that is wide (6.8 km), peaked (rising 700 m over a distance of ~6 km), and consists of a series of en echelon ridge segments (Figure 8b). The vent field is located ~500 m west

Figure 7. (continued)

of the ridge crest and 30 km north of the southern end of a 91 km long ridge segment (Figure 8).

[36] The ultrahigh-resolution bathymetry data reveal a NNE−SSW trending normal fault with 10−15 m throw, that is intersected by a smaller NE−SW fault splay (throw: 4−10 m; Figure 9). The primary fault scarp steps west just north of the intersection with the secondary fault. A small antithetic fault adjacent to the primary fault is evident in the DSL120-A data, and together they bound a narrow triangular sliver of down-dropped seafloor (Figure 9b). There are a number of volcanic domes in the southern portion of the survey area extending over an area of ∼230 m (NE−SW) by 100 m (E−W). Immediately adjacent to the dominant fault scarp, these domes are smaller than those observed at Kilo Moana and Tow Cam (average diameter < 50 m). Lava flows emanating from two domes are identifiable in the bathymetry data at the southernmost extent of the survey area, and many domes have collapse calderas (Figure 9).

[37] Hydrothermal activity was observed at three localized areas at the Tui Malila vent field, extending approximately 350 m both along the major fault scarp that cuts through the area and near its base (Figure 9). The northern area is immediately east of the fault, adjacent to where it is broken into two steps, and contains numerous multispired vent edifices (<4 m tall). Small flanges protruding from the fault scarp, and several very small (<1 m tall) chimneys were observed in this area of hydrothermal activity that extends ∼50 m N−S and ∼30 m E−W. A central area of hydrothermal activity is located approximately 180 m south of the northern area. A diffuse flow site is present in the northern part of this area, a large discrete active flange located ∼8 m east and 60 m south of the diffuse flow area, and there are several vent edifices at the base of the dominant fault (Figure 9b). The southern area, which consists of numerous multiple-spired edifices as well as inactive deposits and hydrothermal sediment, is located approximately 100 m further south and is associated with both the dominant fault and volcanic domes (20−70 m diameter, 4−14 m tall). This area of hydrothermal activity extends ∼100 m N−S and ∼70 m E−W.

[38] Ground-truth observations reveal pillows in the southeastern corner of the survey area and at other localized areas throughout the survey area (Figure 9). These pillows correspond to bumpy textured seafloor with heights of ∼0.5 m over distances of 1.5 to 2 m on sloping seafloor. Near-bottom photos also reveal aa-type flows throughout the survey area, especially associated with finger-like flows (individual fingers 6 m wide, 2 m tall). Sediment cover of variable thickness was observed throughout many portions of the survey area, and
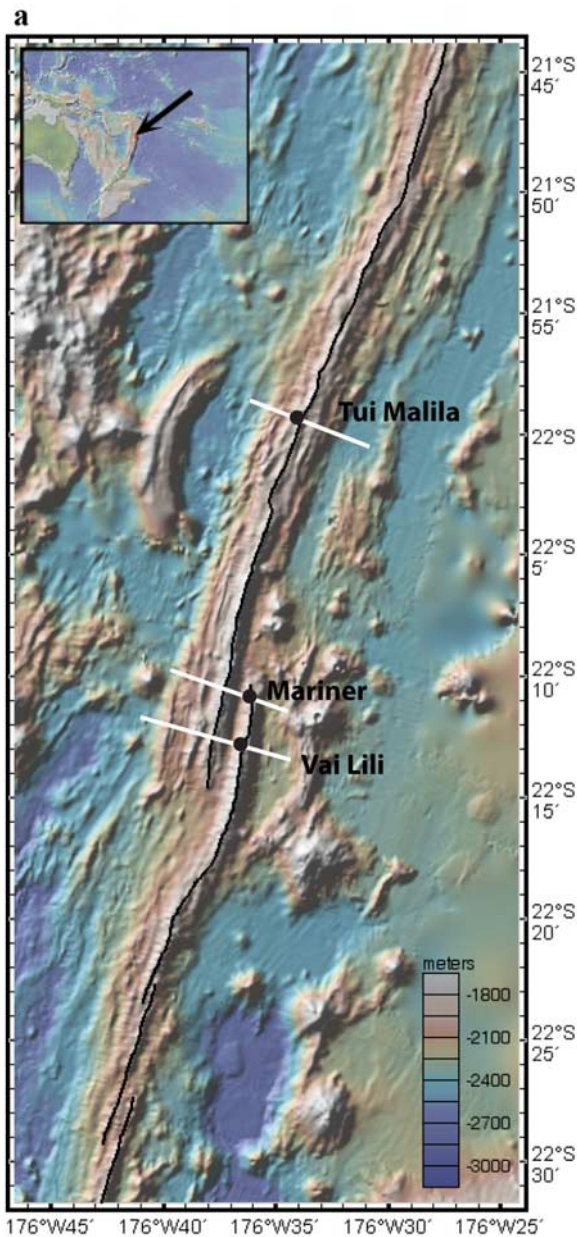
Figure 8. (a) Regional bathymetry of the VFR which hosts the Tui Malila, Mariner, and Vai Lili vent fields. Note that a change in axial morphology occurs north of the overlapping spreading center (OSC) at 22.2°S, with a more peaked ridge south of the OSC. No regional faults or fissures have been identified south of this OSC [*Martinez et al.*, 2006]. The inferred spreading axis is indicated with black lines [*Martinez et al.*, 2006], and vent field locations are identified with black dots. (b) Bathymetric profile across the Tui Malila vent field indicating that the axial ridge is broad (~6.8 km) and tall (~700 m). (c) Bathymetric profile across the Mariner vent field at the OSC. The ridge segment that hosts Mariner is 350 m tall and 1.5 km wide. (d) Bathymetric profile across the Vai Lili vent field. Just 4 km south of Mariner, the axial ridge at Vai Lili is taller (550 m) and wider (2.6 km) than at Mariner.

columnar jointing was observed along the stepped fault scarp in the northern vent area (Figure 9b).

[39] DSL120-A side-scan data indicate that the dominant N–S trending fault that cuts through the vent field extends for at least 7 km. Numerous faults and fissures of varying magnitude dominate the region surrounding the vent field. The region surrounding the vent field also contains localized clusters (hundreds of meters diameter) of small volcanic domes similar to those within the vent field (tens of meters diameter each).

3.5. Mariner

[40] The Mariner vent field, first described by *Ishibashi et al.* [2006], is located on the eastern limb of an overlapping spreading center (OSC) on the VFR (Figure 8a), at 176° 36.09′W, 22° 10.82′S, 1910 m water depth. Mariner is within 2 km of the northern end of the ~350 m tall, 1.5 km wide eastern ridge, and is approximately 250 m west of the ridge crest which is at 1884 m water depth (Figure 8). A NE–SW trending structure that extends ~5 km to the east, across the northern tip of the east limb, might be due to shear within the overlap zone.

[41] Near-bottom bathymetric data at Mariner reveal numerous lava domes with heights of 4–10 m and diameters of 20–40 m (Figure 10). Most of these domes are flat-topped, and some have craters. Other prominent bathymetric features are tall (10–27 m) narrow hydrothermal edifices that are not branched but instead taper [*Tivey et al.*, 2005]. Flow fronts emanating from the east are evident west of the hydrothermal pinnacles, some of which have finger-like morphology (1 m tall, 10 m wide) that is not as well defined as at ABE and Tui Malila (Figure 9), in part because they are obscured by the domes that dominate the vent field. Compared with vent fields to the north, local faults and fissures are notably absent at Mariner.

[42] Hydrothermal activity at Mariner is primarily associated with vent pinnacles with hot (342–363°C) fluids emanating from close to their bases and part way up their sides [*Tivey et al.*, 2005] (Figure 10). Visual observations show that some localized areas of lower temperature flow, from tabular, squat edifices are present E–NE of the hydrothermal pinnacles. Areas of variable sediment cover were observed throughout the area on what appears to be primarily aa-type flows (Figure 3d).

[43] The DSL-120A data reveal that the volcanic domes of the Mariner field are part of a linear series
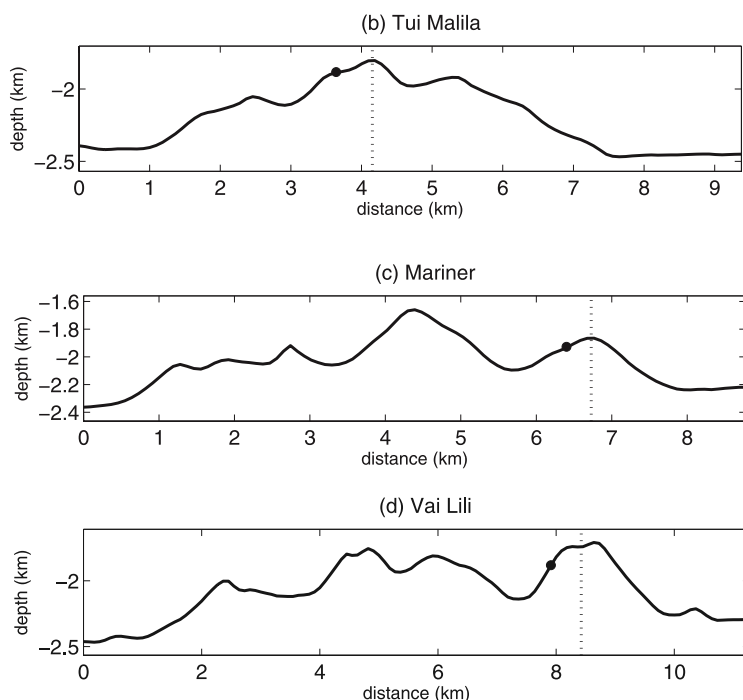
Figure 8. (continued)

of domes (30–60 m diameter) extending ~1 km N–S. These domes are generally within 100 m of the ridge crest and are parallel to it. No regional faults or fissures are evident near Mariner.

3.6. Vai Lili

[44] The Vai Lili vent field is located at 176° 36.50′W 22° 12.91′S, 1720 m depth (Figure 8a), and was first identified by *Fouquet et al.* [1991]. Just 4 km south of Mariner, and associated with the same ridge segment within the OSC on the VFR, the ridge is taller (550 m) and wider (2.6 km) at Vai Lili (Figure 8). At this latitude, the two segments of overlapper are 2.7 km apart, and the eastern limb that hosts Vai Lili is a well-defined symmetric ridge 2.2 km wide and 250 m high, 50 m shallower than the adjacent flanks (Figure 8).

[45] At least six closely spaced cratered domes oriented N–S are evident in the southern half of the survey area spanning a distance of ~100 m (Figure 11). Individual flows emanating from many of these domes can be identified in the bathymetric data, and one ~4 m thick flow that extends toward the west can be traced to the largest dome/crater at the southern extent of the survey area (Figure 11). The heights and widths of many of these domes are difficult to quantify because they are obscured by flows that have been emplaced around them, but

well-defined craters are evident. Immediately north of the large dome in the south are what appear to be three volcanic ridges that extend N–S for ~100 m (Figure 11).

[46] Further to the north, a relic eruptive fissure (<~8 m wide, 2.5 m deep) runs N–S through the survey area, and is adjacent to scalloped flow fronts (Figure 11). North and east of the eruptive fissure are at least seven additional domed features, four of which have craters. A NE–SW trending fault with ~1 m throw) cuts through one of these domes. Although ground-truth observations at Vai Lili are spatially limited, localized areas of sediment with variable thickness were observed in the southwest portion of the survey area.

[47] Hydrothermal activity at Vai Lili in 2005 consisted of 121°C fluid pooled beneath marcasite-lined flanges [*Tivey et al.*, 2005; M. K. Tivey, manuscript in preparation, 2008], and 70°C clear fluid emanating from a small Fe-oxide chimney. No higher temperature venting was observed in 2005, but many large sulfide mounds and relic flanges were identified along the small volcanic ridges. A series of andesitic plugs that extend N–S were observed approximately 20 m west of the area of where relic sulfide edifices and active venting were observed. Two areas of diffuse flow were
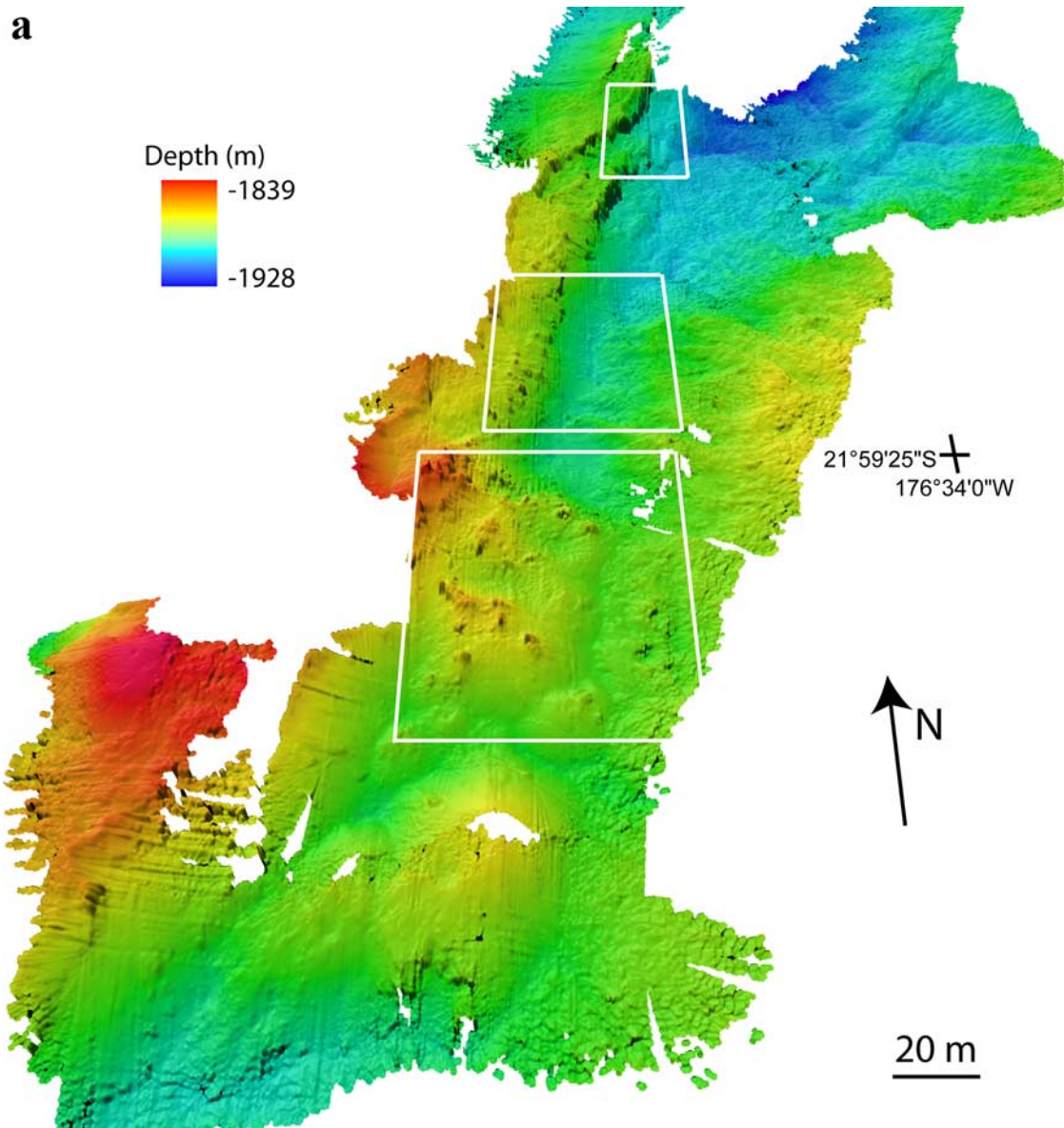
Figure 9. (a) Tui Malila vent field on the VFR. Perspective view of ultrahigh-resolution bathymetry data. Note that areas of hydrothermal activity (white boxes) are located close to the dominant fault scarp, and some are associated with volcanic domes. The bumpy texture in the southeastern extent of the survey area is due to pillow lavas. (b) Geologic interpretation of bathymetric features nested within DSL120A side-scan data [*Martinez et al.*, 2006]. Hydrothermal vents identified in this view include both active and inactive edifices. Areas of low backscatter intensity are dark, and areas of high backscatter intensity are light. Several flow fronts are identifiable at Tui Malila, most of which appear to have been sourced from the east. Columnar jointing was observed at one location along the fault scarp within the northern area of hydrothermal activity.

observed near the small fault in the northeast portion of the survey area (Figure 11).

[48] Numerous cratered domes can be identified in the DSL120 data in the area surrounding the vent field, and ~150 m north of the vent field (Figure 11b). An area of high backscatter intensity that intersects the SM2000 coverage has morphology that resembles a lava channel. Although lava channels at the EPR are characterized by low backscatter intensity [*Soule et al.*, 2005] this feature is characterized by high backscatter intensity (Figure 11b). This could be due, in part, to increased roughness associated with
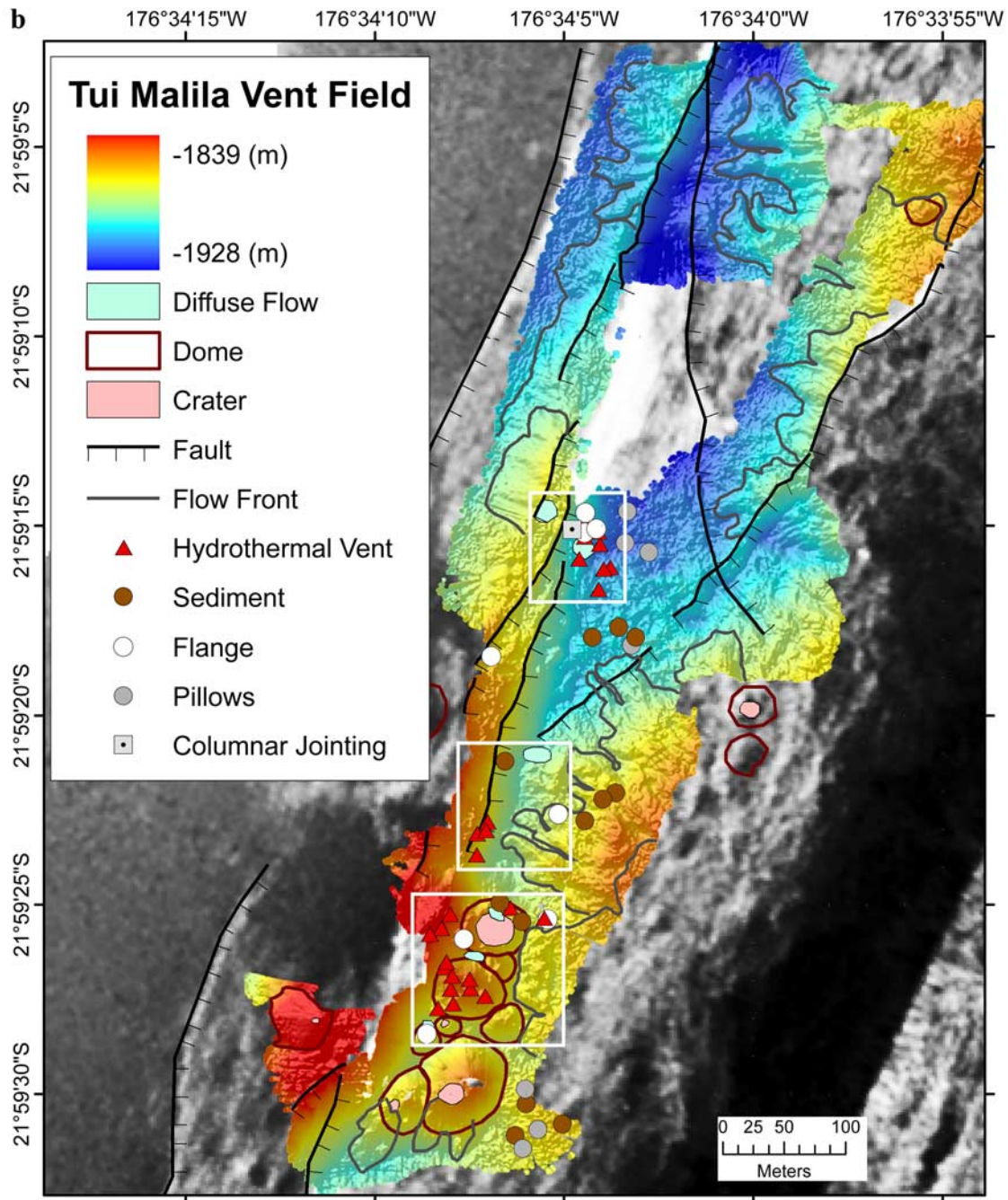
Figure 9. (continued)

silica-rich flows on the VFR [*Fouquet et al.*, 1993; *Fretzdorff et al.*, 2006] compared with the sheet-like basaltic flows that dominate EPR lava channels [*Soule et al.*, 2005]. A lack of sediment cover on this rough surface would result in relatively high backscatter intensity compared with more heavily sedimented areas surrounding it.

[49] Many acoustic backscatter features to the north and south of the vent field appear to be individual westward flowing lava flows. Faults and fissures that are parallel to the ridge crest are evident in the regional side-scan data within hundreds of meters of the vent field primarily to the east. Larger domes (<~200 m diameter) with collapse craters (<~100 m diameter) are evident
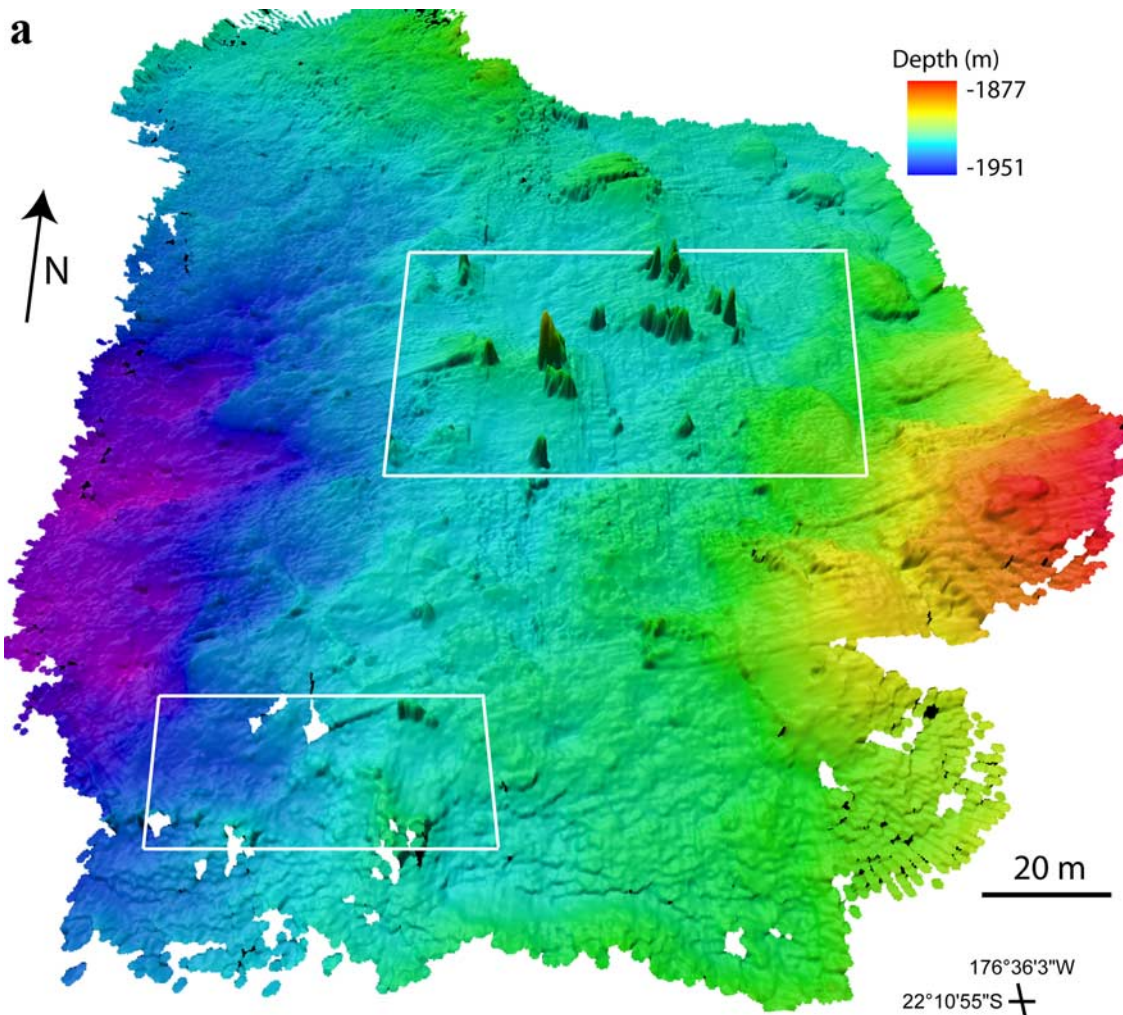
Figure 10. (a) Perspective view of Mariner vent field on the VFR revealing multiple dome structures and large vent edifices (10–27 m tall). Areas of observed hydrothermal activity are outlined with white boxes. (b) Geologic interpretation of ultrahigh-resolution bathymetry nested within DSL120A side-scan data [*Martinez et al.*, 2006]. Areas of low backscatter intensity are dark, and areas of high backscatter intensity are light. Numerous high aspect ratio volcanic domes are evident within the vent field and in the area surrounding it. Finger-like flows are evident at Mariner, but are not as well defined as at Tui Malila and ABE.

for at least 2 km south of Vai Lili, while smaller (tens of meters) cratered domes are evident to the north.

4. Results 2: Roughness Analysis

[50] Rugosity grids computed for 20×20 m areas of known volcanic morphology and reveal quantitative differences in seafloor roughness. Heavily sedimented areas and sheet flows reveal spatially continuous areas of low rugosity with values generally less than 1.1 (Figure 12a). By contrast, rugosity grids of pillow/lobate terrain show higher rugosity values (1.1 to 2) associated with the edges of individual volcanic pillows and lobes (Figure 12b). Spatially continuous areas of higher rugosity (generally > 2) are associated with flow fronts, with values dependent on the thickness of the flow (Figure 12c). Finally, the rugosity grids computed for faults/fissures generally reveal semilinear spatially continuous areas of high rugosity values resulting from steep slopes associated with fault scarps and fissure edges (Figure 12d).

[51] Systematic differences in the magnitude and variability of rugosity characteristics for each seafloor type are evident by comparing average frequency distributions for each site (Figure 13a). For
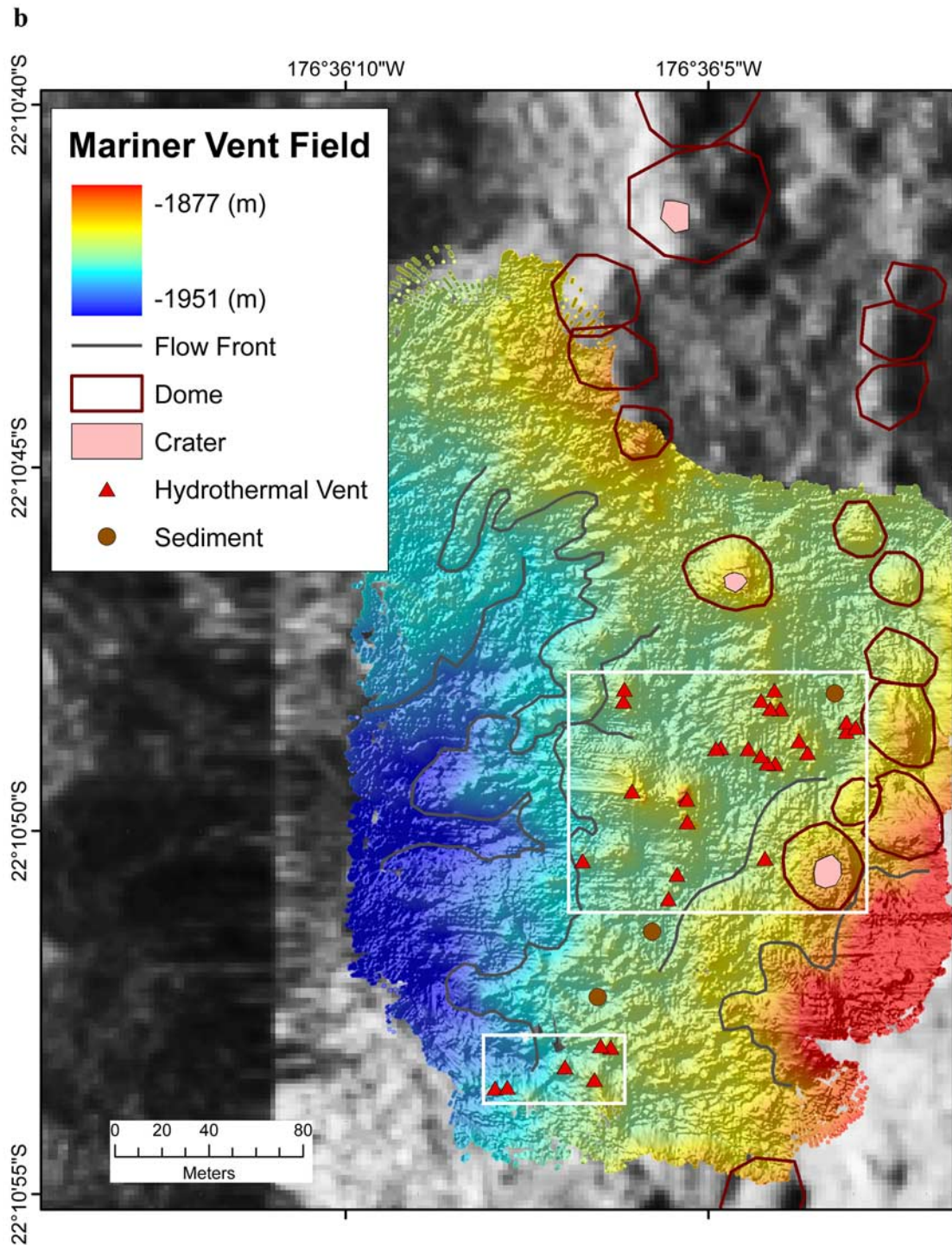
Figure 10. (continued)

pillows/lobate terrain, faults/fissures, and finger-like flow fronts these curves were computed with five 20 × 20 m areas from each site, but for heavily sedimented areas at ABE and sheet flow observed at EPR, two 20 × 20 m rugosity grids were used because of limited observations. Boxplots of

graphic mean and graphic standard deviation based on all cumulative percentage curves further elucidate these differences, and provide an indication of the consistency of rugosity characteristics within each site and seafloor type (Figures 13b and 13c).
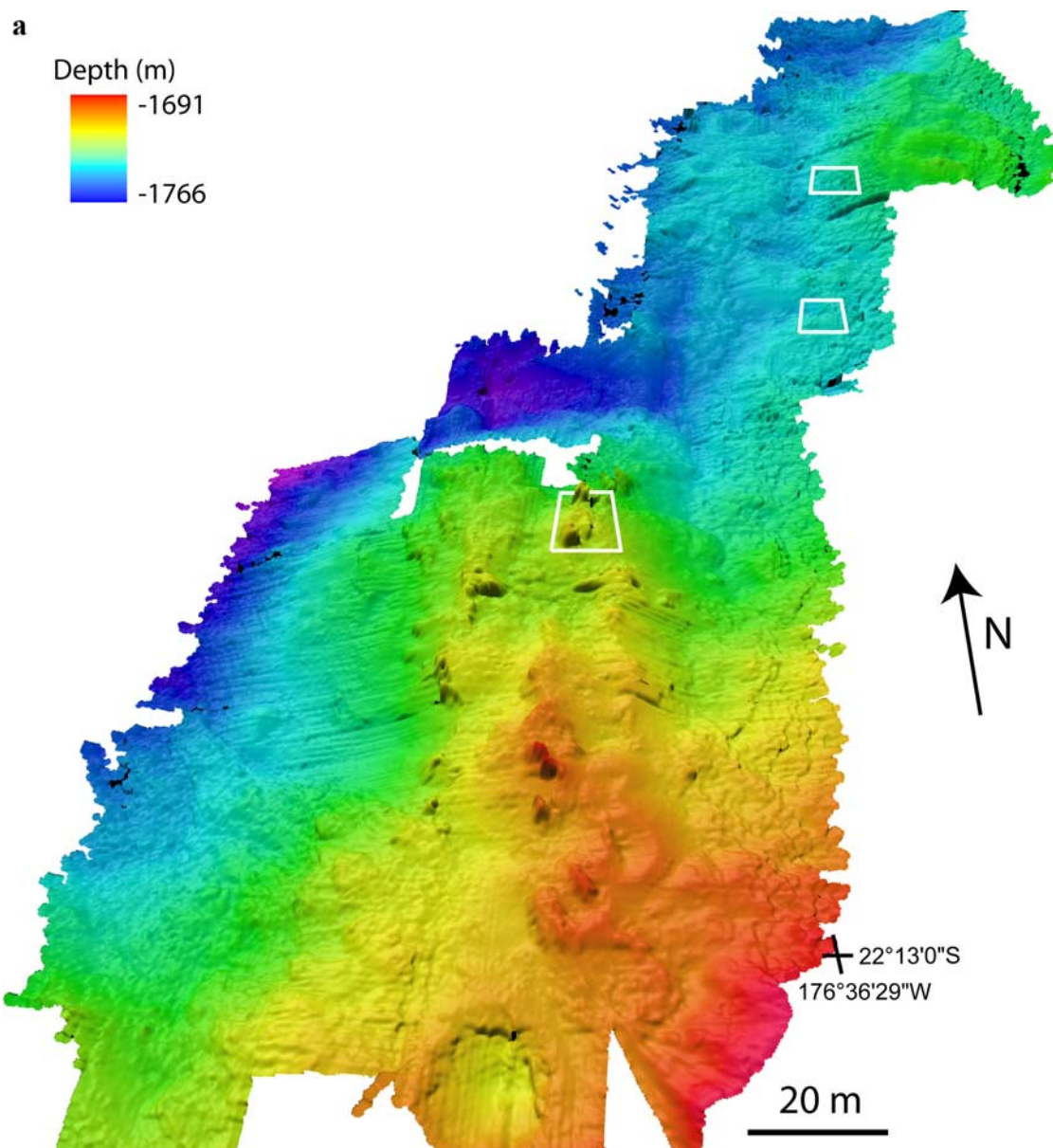
Figure 11. (a) Vai Lili vent field on the VFR. Perspective view of ultrahigh-resolution bathymetry revealing numerous cratered domes in the southern extent of the survey area. Note the distinct flow emanating toward the N–NW from the southernmost cratered dome. Observed areas of hydrothermal activity (both focused and diffuse flow) are outlined with white boxes. (b) Geologic interpretation of ultrahigh-resolution bathymetry nested within DSL120A side-scan data [*Martinez et al.*, 2006]. Areas of low backscatter intensity are dark, and areas of high backscatter intensity are light. In addition to numerous domes, there appears to be a relic eruptive fissure and parallel volcanic ridges. Nested within the DSL120A data, it is clear that the volcanic domes that dominate Vai Lili extend for hundreds of meters to the north and south. A backscatter feature that resembles a lava channel may be evidence of recent volcanic activity at Vai Lili.

[52] Seafloor morphology characterized by small-scale vertical relief (pillows/lobates and sediments/sheet) is clearly distinct from morphologies with larger vertical changes (flow fronts and faults/fissures). Along-axis variability in volcanic morphology that might be related to changes in substrate characteristics is also evident, with rugosity

of pillows/lobates in dominantly basaltic substrate (Kilo Moana, Tow Cam [*Bezos et al.*, 2005]) having lower values than similar morphologies identified in more silica-rich and vesicular lavas (ABE, Tui Malila [*Bezos et al.*, 2005]). This trend is also evident when including data from the EPR (Figure 13). Changes in the morphologic character-
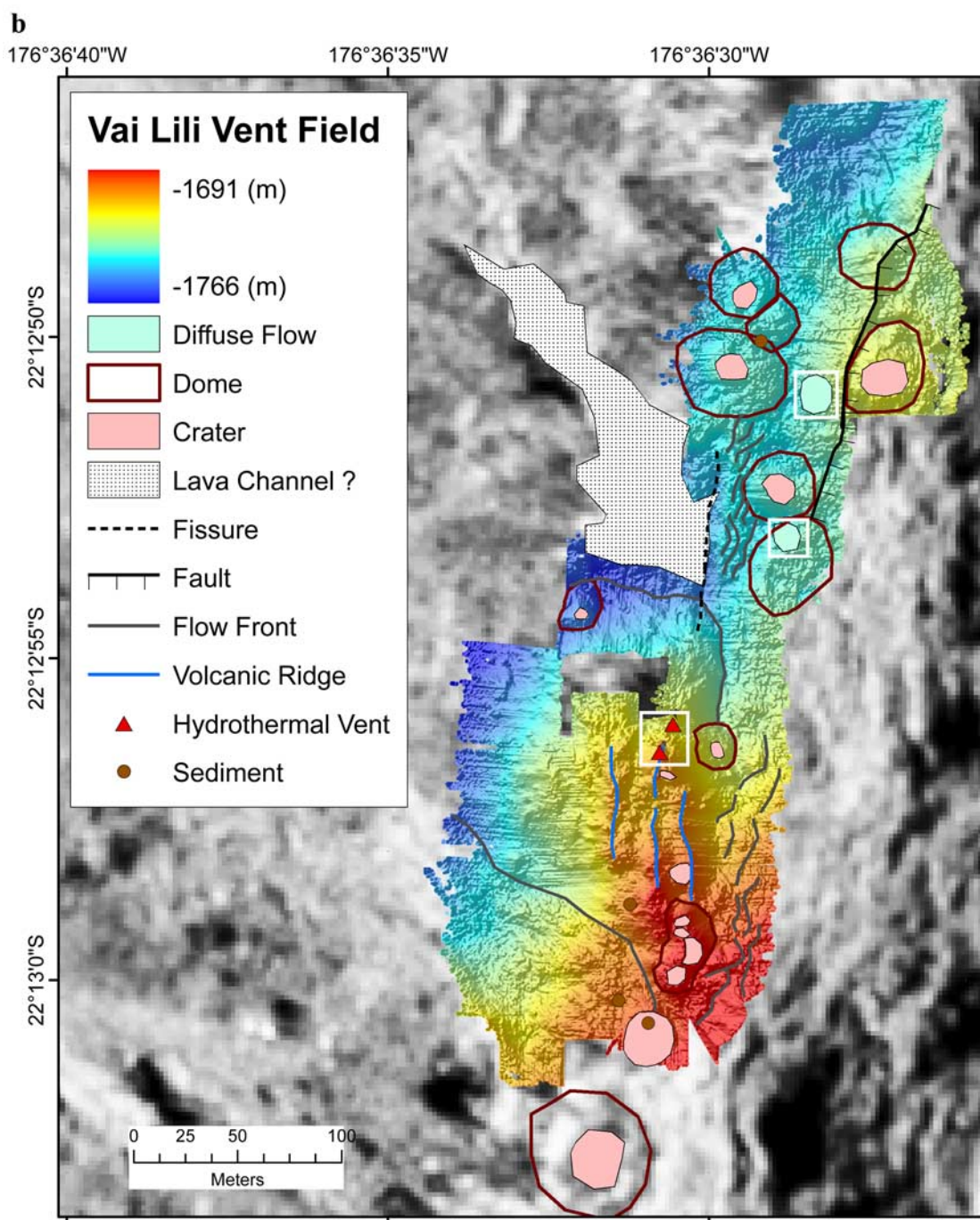
Figure 11. (continued)

istics of finger-like flows are also quantified with rugosity characteristics, with tall narrow finger-like flows at ABE (~4 m tall, ~4 m across) distinct from the flatter, wider flows at Mariner (~1 m tall, ~10 m across).

[53] The observed differences in rugosity characteristics of 20 × 20 m areas of known morphology

(Table 1 and Figure 13) were used to perform a supervised classification of the ultrahigh-resolution map from each vent field using a 5 × 5 m window passed through each bathymetric grid at a spacing of 2 m (Figure 14). A rugosity grid, and its frequency distribution, was computed only when the window was fully populated with data (i.e., no data gaps). Given this constraint, a 20 × 20 m
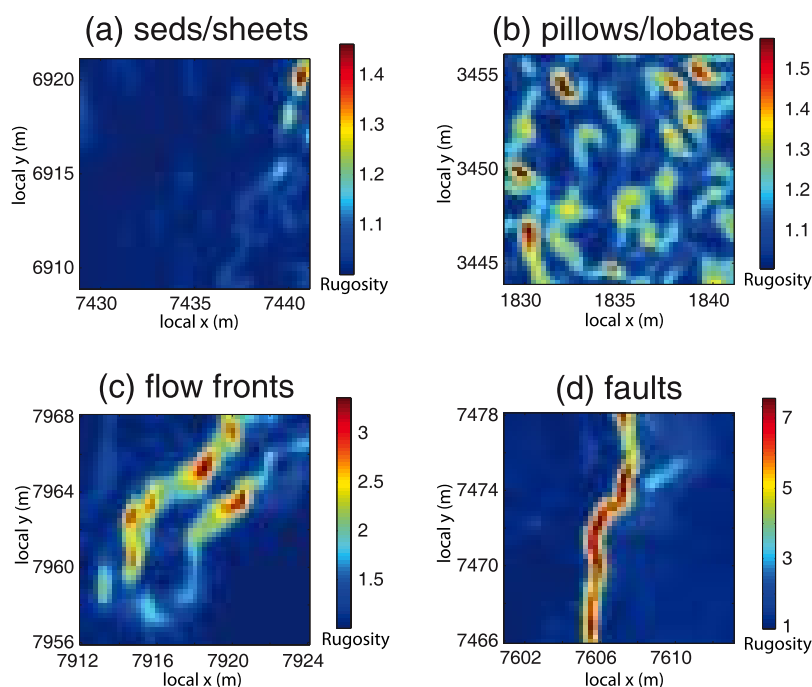
Figure 12. Example rugosity grids computed for 20 × 20 m areas of known seafloor morphology: (a) heavily sedimented area at ABE, (b) pillow lavas at Tui Malila, (c) finger-like flow front at ABE, and (d) fault scarp at Tui Malila. Note differences not only in the magnitude of rugosity values but also in the rugosity patterns associated with each morphology type.

window resulted in a classification with discontinuous spatial coverage. Using a 5 × 5 m window, however, yielded an equivalent classification but at higher spatial resolution, providing better continuity of features.

[54] This classification successfully identified faults and fissures with vertical relief greater than 4 m at Kilo Moana, Tow Cam, ABE, and Tui Malila (Figure 14). Broad areas of pillow/lobate terrain are also identified at these sites, as were some finger-like flow fronts and edges of pillow/lobate flows. Regions of heavy sediment cover near the NW and SW extent of the ABE survey area were successfully identified and are distinct from most pillow/lobate terrain, with the exception of relatively flat smooth areas of lobate terrain (e.g., Tow Cam). No attempt was made to identify the larger-scale morphologic features (e.g., domes and craters) observed at Mariner and Vai Lili.

5. Discussion

5.1. Along-Axis Trends

[55] Comparisons of tectonic and volcanic features and their relationships to hydrothermally active areas at six vent fields along 245 km of the ELSC

and VFR reveal along-axis gradients in volcanic and tectonic morphology that provide insight into the nature of the hydrothermal systems. An along-axis gradient in volcanic morphology from north to south is evident, with the northern two vent fields dominated by pillow and lobate terrains on broad low-relief volcanic domes (hundreds of meters wide, <10 m tall), the central two vent fields characterized by variable terrain composed of pillows and rough rubbley aa-type volcanic terrain and finger-like flow fronts, and the southern two vent fields dominated by aa-type flows, smaller and higher relief volcanic domes (tens of meters wide, tens of meters tall) and some finger-like flows. The increase in the abundance and aspect ratio of volcanic domes toward the south coincides with observed changes to more silica rich lava composition [*Pearce et al.*, 1995; *Bezos et al.*, 2005] and an increase in volcanic productivity [*Martinez et al.*, 2006]. Changes in local volcanic morphology also coincide with marked changes in the large-scale morphology of the ridge axis where the spreading center transitions from an axial valley north of ABE to an axial ridge to the south [*Martinez et al.*, 2006; *Jacobs et al.*, 2007].

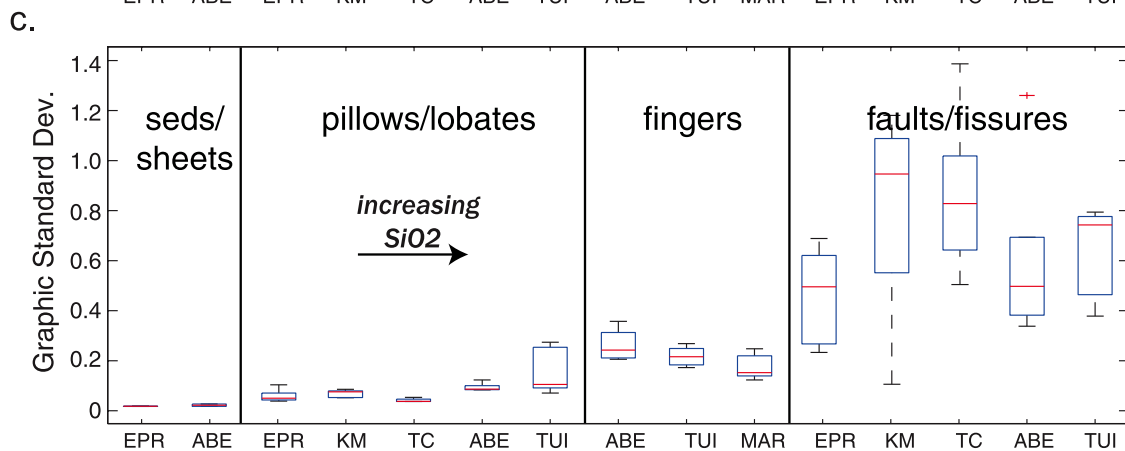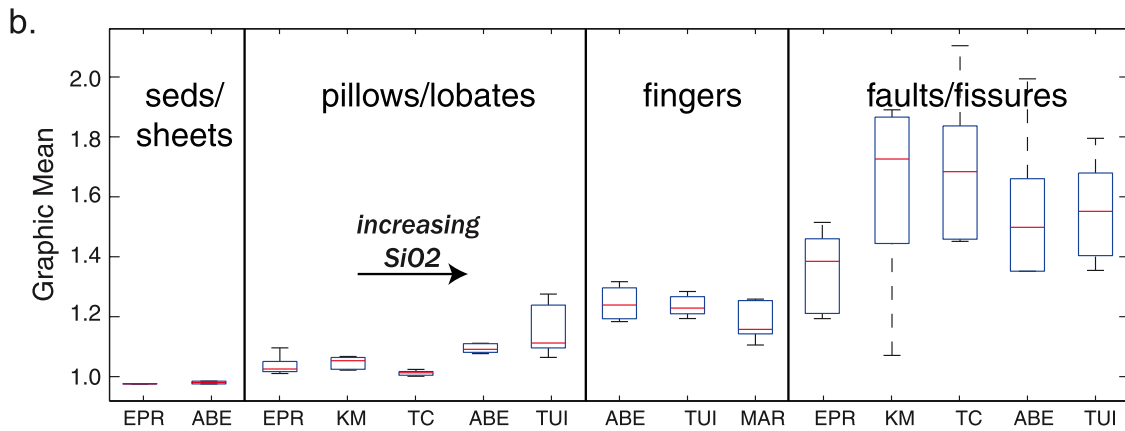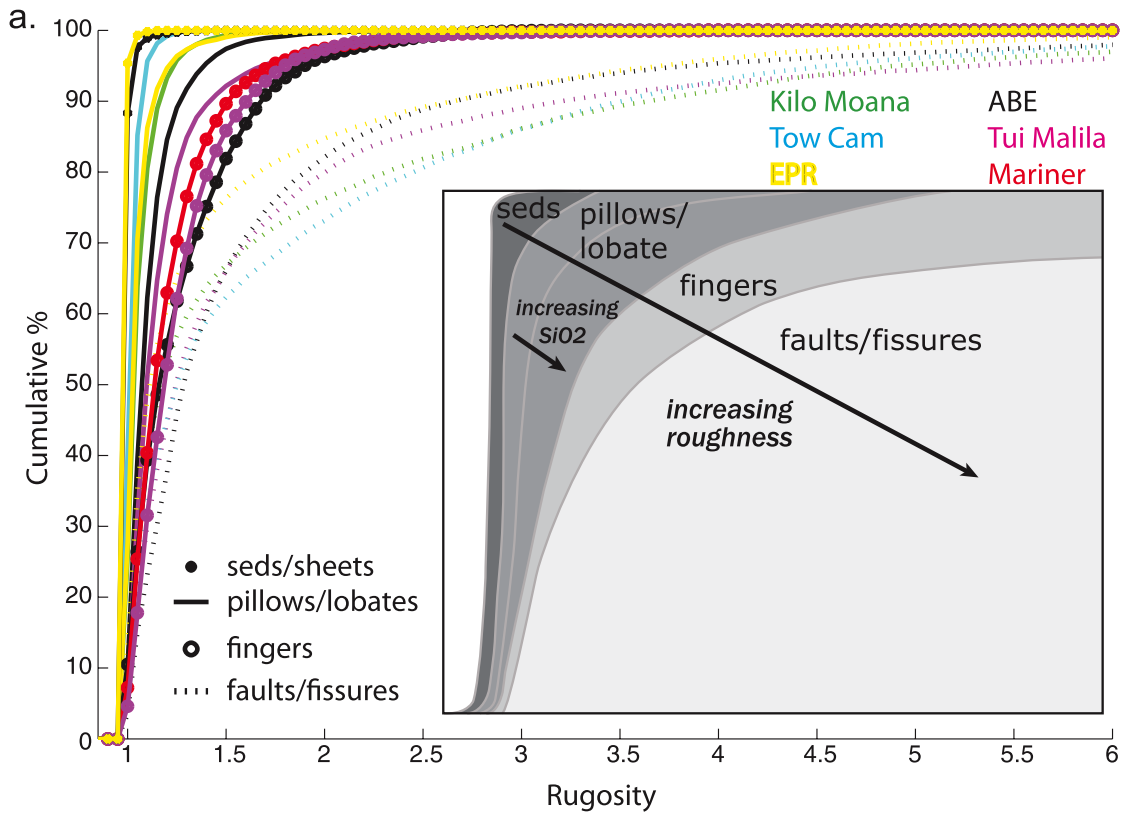[56] The decrease in faulting and fissuring toward the south that has been observed in regional side-

Figure 13

Table 1. Graphic Statistics of Rugosity Used to Classify Morphologic Features

Morphology	Graphic Mean	Graphic Standard Deviation
Sediment	<1	<0.04
Pillows/lobate terrain	1–1.1	0.04–0.16
Flow fronts	1.1–1.2	0.16–0.25
Faults/fissures	>1.4	>0.25

scan and bathymetry data [*Martinez et al.*, 2006] is also evident in our ultrahigh-resolution bathymetry maps, which better define a significant transition in this trend by revealing a lack of surface-expressed faults and fissures at vent fields south of the OSC at 22.2°S. Decreased faulting is evident on the ridge flanks as well as within the axial region, and hence cannot be simply attributed to differences in time since last volcanic repaving of the axial region. Rather, differences in the rheology and thickness of the brittle upper crust are implied. Differences in faulting linked to eruption processes may also contribute [e.g., *Carbotte et al.*, 2006]. For example, faulting during dike intrusion could be an important process in the north whereas the abundant volcanic domes in the south suggest more localized point source volcanism in this region. The correlation of observed areas of hydrothermal activity with faults and fissures at vent fields north of the OSC (Kilo Moana, Tow Cam, ABE, and Tui Malila) suggests that hydrothermal circulation in those vent fields is focused by tectonic structures. By contrast, the southern two vent fields (Mariner and Vai Lili) are hosted within volcanic terrain with abundant high aspect ratio volcanic domes with collapse calderas, and little to no surface expression of faults and fissures. In these regions, permeable pathways in these volcanic structures associated with volcanic emplacement processes may control the subsurface architecture of hydrothermal circulation.

[57] The along-axis differences we observe in fine-scale volcanic and tectonic morphology are correlated with changes in the physical properties of the upper crust inferred from seismic observations [*Jacobs et al.*, 2007]. At the northern two vent sites, the thickness and compressional wave velocity of the uppermost crust, seismic layer 2A, are similar to values typically found at intermediate spreading mid-ocean ridges (layer 2A $\sim$ 400–500 m thick; velocity $\sim$2.7 km/s). No axial magma chamber (AMC) has been imaged beneath these vent fields [*Jacobs et al.*, 2007], but a short mushy AMC reflection has been identified north of Kilo Moana [*Jacobs et al.*, 2006]. The transition from an axial valley to axial high in the vicinity of the ABE vent field marks a transition in seismic properties: a discontinuous AMC reflector is present ($\sim$2.25 km below seafloor), the thickness of layer 2A increases, and velocities within both layer 2A and 2B decline. Along the VFR, the subseafloor depth of the AMC increases toward the south from a depth of $\sim$2.2 km near Tui Malila to $\sim$2.7 km near Mariner and Vai Lili. The thickness of layer 2A increases, to $\sim$800 m near Mariner and Vai Lili, and an along-axis decrease in layer 2B velocities is also evident with velocities as low as 4.0 km/s on the VFR, compared with the more typical 2B velocities of 5 km/s along the CLSC (2B velocities are not resolved near Kilo Moana and Tow Cam). *Jacobs et al.* [2007] attribute these changes in layer 2A and 2B characteristics to differences in rock mineralogy and increased intrinsic porosity due to higher volatile presence within magmas with proximity to the volcanic arc.

[58] Located 28.5 km apart, the Kilo Moana and Tow Cam vent fields are on different segments of the N-ELSC, but both are hosted in pillow and lobate terrain on broad low-relief volcanic domes. Individual flow fronts are not evident in the ultrahigh-resolution bathymetric maps or in the regional DSL-120A side-scan data. Little sediment cover was observed at these vent fields suggesting that the seafloor is relatively young. Since faults and

Figure 13. (a) Site-averaged cumulative percentage rugosity curves revealing systematic differences between different lava morphologies. Each average curve for pillows/lobate flows, finger-like flows, and faults/fissures was generated with five 20 × 20 m areas of known seafloor morphology, while average curves for sediment and sheet flows are based on two 20 × 20 m areas each. Boxplots of (b) graphic mean and (c) graphic standard deviation values generated from all rugosity grids computed for all morphology types observed at each vent field. Relatively smooth sheet flows and heavily sedimented areas typically have the lowest rugosity values and show little variance compared with other morphology types. Pillows/lobate flows have higher rugosity values and larger variance. Faults/fissures exhibit the highest values and the most variability. Note that differences in rugosity associated with substrate type are also apparent, with pillows/lobates in more silica rich substrate (Tui Malila, ABE) characterized by higher values than those in basaltic substrate (Kilo Moana, Tow Cam, EPR).
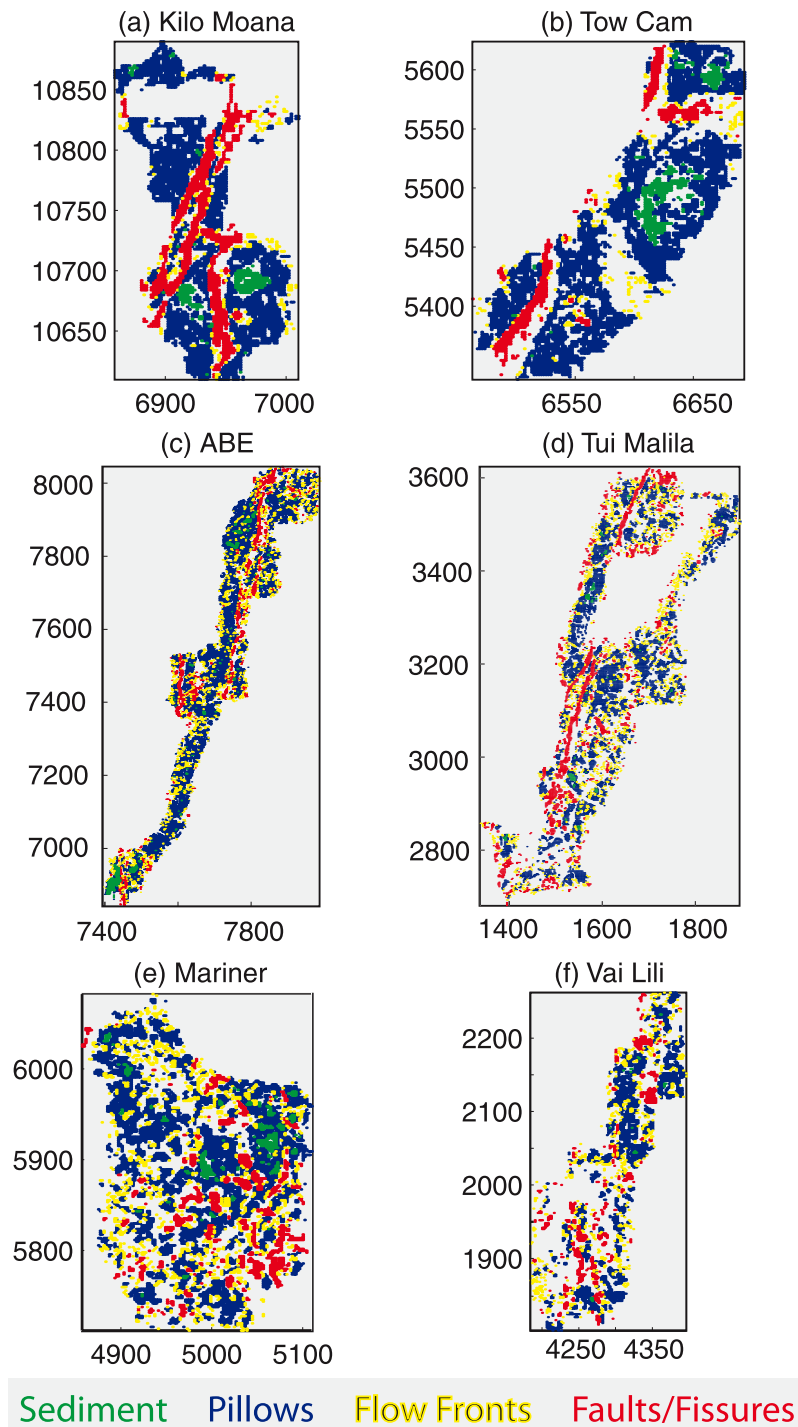
Figure 14. Rugosity classification of ultrahigh-resolution maps based on graphic mean and graphic standard deviation values derived from areas of known morphology (Figure 12 and Table 1). This classification was done using a 5 × 5 m moving window with nodes spaced 2 m apart to compute rugosity. Axes are meters in local XY coordinates (http://www.whoi.edu/page.do?pid=22235). Large faults and fissures (>4 m vertical relief) are successfully identified (red) using this classification scheme, as are areas of pillows/lobate terrain (blue) and heavily sedimented areas (green).

fissures cut many domes at these sites, it is clear that volcanic activity predates tectonic activity. At both vent fields, hydrothermal activity is localized at the bases and tops of fault scarps and fissures (throw: 1–20 m). The physical relationships between areas of venting and faults and fissures are consistent with hydrothermal circulation being focused by tectonic features.

[59] Although physically closer to the Tow Cam vent field (50 km), the ABE vent field is more similar to Tui Malila, which is located 141 km further south on the VFR. Volcanic morphology within the ABE and Tui Malila vent fields is more variable and complex than at the northern two vent fields, with observations of pillows and aa-type lavas, and distinct flow fronts. The directionality of flows observed at these vent fields indicates that most were sourced from the east, consistent with the location of these vent sites on the western slope of the axial high. Many flows at these vent fields are cut by faults indicating that tectonic activity postdates volcanic activity, but variable sediment cover indicates that lava has been emplaced over variable timescales. Visual observations of areas with little sediment cover at ABE suggest that some flows may be young.

[60] Observations of areas of heavy sediment cover in portions of ABE, which is located near a left stepping offset composed of small en echelon segments, is consistent with less frequent eruptions occurring near segment ends [*White et al.*, 2002]. Columnar jointing identified along stepped fault scarps (throw: 4–20 m) at both ABE and Tui Malila indicates that some lava flows within these vent fields were emplaced as thick units indicating large volume eruptions. This type of columnar jointing has been observed in a deep fissure at the Cleft Monolith Site [*Chadwick et al.*, 2001], but has not been observed on fault scarps at other spreading centers.

[61] Volcanic domes evident at or near the ABE and Tui Malila vent fields have higher aspect ratios than those at Tow Cam and Kilo Moana, likely due to changes in lava viscosity associated with increased silica content [*Pearce et al.*, 1995; *Bezos et al.*, 2005; *Jacobs et al.*, 2007]. The vertical thickness of discrete finger-like flows (3–4 m), and observed increases in rugosity associated with pillows at ABE and Tui Malila are further evidence of higher viscosity lava than at the northern sites.

[62] Active hydrothermal vents and areas of diffuse flow at ABE and Tui Malila are localized along and adjacent to faults, suggesting that hydrothermal circulation is focused by tectonic features. Some hydrothermal vents at Tui Malila are associated with small volcanic domes and hydrothermal circulation may also be focused by permeable pathways in volcanic structures.

[63] The Mariner and Vai Lili vent fields are located just 20–26 km south of Tui Malila, on the southern limb of the OSC at 22.2°S. Seafloor morphology at these vent fields is dominated by small (tens of meters diameter) domes, many of which have collapse craters indicating magmatic point sources. These domes are distinct from the broad domes found at Kilo Moana and Tow Cam, but are similar to those observed at Tui Malila. Flow fronts are identifiable at both vent fields, with finger-like flow fronts at Mariner, and distinct flows traceable to individual cratered volcanic domes and an eruptive fissure at Vai Lili. The relative increase in volcanic relief that we observe at Mariner and Vai Lili, as well as the dominance of aa-type lava flows, suggests an increase in lava viscosity, and is consistent with a transition to more silica-rich substrate toward the south [*Pearce et al.*, 1995; *Bezos et al.*, 2005]. No pillows or lobate flows were observed at these sites, but ground-truth observations are spatially limited.

[64] The lack of faults cutting volcanic features at Mariner is consistent with regional observations of fewer tectonic features in this region [*Martinez et al.*, 2006]. The tall (10–27 m), narrow, localized hydrothermal vent edifices, and the observation of active venting near the base and on the sides of the pinnacles suggests sustained localized hydrothermal activity that has not been interrupted by tectonic processes. Observations of heavy sediment cover in parts of the Mariner vent field indicate that no recent volcanic flows have been emplaced at the vent field.

[65] Although a single fault was noted at Vai Lili, most volcanic features appear unaltered by tectonic processes. Seafloor imagery collected during our mapping and sampling program reveals variable (and locally heavy) sediment cover but no evidence of recent volcanic activity. Although bottom photos collected in the vicinity of Vai Lili in 2004 show evidence of recent localized volcanic activity [*Fretzdorff et al.*, 2006], none of our ground-truth observations confirm the location of this with respect to our survey area. A backscatter feature in the DSL120A side-scan data, however, that morphologically resembles a lava channel (Figure 9d), may be evidence of a recent localized eruptive

event at Vai Lili; high backscatter in this area is indicative of a lack of sediment cover relative to surrounding areas.

[66] With the absence of major faults and fissures within the Mariner and Vai Lili vent fields, there is little evidence that hydrothermal activity at these fields is focused by tectonic structures. The abundance of volcanic domes at these vent fields, many of which have collapse craters, instead suggests that hydrothermal circulation is focused by permeability within these volcanic structures linked to volcanic emplacement processes. Connected porosity associated with lava flow contacts and volcanic collapse may provide primary pathways for hydrothermal circulation. The compositions of fluids sampled at Mariner in 2005 are volatile-rich compared to those sampled from the northern vent fields, and is consistent with hydrothermal activity being more directly related to volcanic processes [*Seewald et al.*, 2005; *Proskurowski et al.*, 2007].

5.2. Roughness Analysis

[67] Ultrahigh-resolution bathymetry maps allow us to quantify the dimensions of tectonic, volcanic and hydrothermal features, and also reveal their physical relationships to one another. Observed differences in fine-scale seafloor roughness associated with sedimented areas and pillow/lobate terrain suggest that maps of submeter resolution can also provide information about seafloor morphology that until now was only discernable through visual observations of the seafloor. If variations in seafloor roughness associated with different lava morphologies can be quantified in ultrahigh-resolution bathymetric maps, the information can aid in detailed mapping of lava flows and will improve our understanding of lava emplacement and crustal formation.

[68] Using rugosity to quantify seafloor morphology relies almost exclusively on the magnitude of roughness. Perhaps the most significant finding of the rugosity analysis is that the bumpy texture of pillow and lobate terrain is quantitatively distinct from heavily sedimented areas that appear smooth in ultrahigh-resolution maps. This confirms that the bumpy texture we observe is caused by physical features on the seafloor, not sonar artifacts. A variety of other surface roughness parameters [e.g., *Stout*, 2000] could be used to quantify small-scale bathymetric variability associated with pillows and lobate terrains and large-scale changes associated with faults and fissures, but computing graphic statistics of the rugosity distribution pro-

vides a means of assessing the spatial consistency of rugosity. Observed differences in rugosity values computed for pillow and lobate terrain in basaltic substrate (Kilo Moana, Tow Cam, and EPR) compared with more silica-rich and vesicular substrate (ABE, Tui Malila), suggest that these data might also be useful for mapping variations in lava composition.

[69] The development of robust seafloor characterization tools will require the analysis of additional data sets that are well-constrained with respect to survey parameters, and are supplemented with both visual ground-truth observations and seafloor samples. Well-constrained surveys may provide sufficient information to distinguish pillows and lobate terrain from aa-type flows on the basis of the regularity of roughness. Techniques for characterizing flow fronts, faults and fissures will require additional parameters that consider not only the magnitude, but also the directionality and continuity of roughness. The success of any roughness classification method will require careful consideration of not only the scale of roughness, but also the scale of the area over which roughness statistics are computed. As a result, a multiscalar classification approach may be necessary.

6. Conclusions

[70] Ultrahigh-resolution bathymetric maps of hydrothermal vent fields permit the quantification of the dimensions and physical relationships between tectonic, volcanic and hydrothermal features and provide insight into the nature of hydrothermal systems. The along-axis trends in ultrahigh-resolution bathymetry that we document are consistent with observations of regional volcanic and tectonic setting, proximity to the arc front [*Martinez et al.*, 2006], and along-axis changes in geochemical composition and physical properties of the substrate [*Pearce et al.*, 1995; *Bezos et al.*, 2005; *Jacobs et al.*, 2007].

[71] A marked transition in volcanic morphology occurs between the Tow Cam and ABE vent fields, where the axial morphology transitions from an axial valley to an axial ridge, and seismic characteristics of the upper crustal support a transition to more silica rich higher porosity andesitic lavas [*Jacobs et al.*, 2007]. Vent fields north of this transitional area (Kilo Moana and Tow Cam) are dominated by pillow and lobate terrain with broad flat domes that are cut by faults and fissures, while

southern vent fields (ABE, Tui Malila, Mariner, Vai Lili) are characterized by more complex volcanic morphology with pillows, aa-type flows, distinct flow fronts, and larger aspect ratio domes.

[72] Along-axis changes in volcanic morphology, magmatic activity [*Martinez et al.*, 2006], substrate composition [*Bezos et al.*, 2005; *Jacobs et al.*, 2007], and the lack of faults and fissures at vent fields within the OSC 22.2°S, indicate along-axis differences in hydrothermal circulation pathways. While hydrothermal circulation at the northern two vent fields (Kilo Moana and Tow Cam) appears to be focused by faults and fissures, hydrothermal circulation at the southern two vent fields (Mariner and Vai Lili) is likely through permeable pathways in volcanic structures associated with lava flow contacts. Characteristics of the central two vent fields (ABE and Tui Malila) indicate that hydrothermal circulation is likely associated with both tectonic focusing and permeable pathways in volcanic structures.

[73] Quantitative differences in rugosity computed with the ultrahigh-resolution maps provide an important first step toward remote characterization of the complex terrains associated with hydrothermal vent fields. Differences between sedimented areas and pillow/lobate terrain demonstrate that near-bottom mapping technology has evolved sufficiently for quantitative measurements of the seafloor at submeter resolution. Although rugosity statistics can be used to identify gross differences in seafloor morphology based primarily on the magnitude (graphic mean) and consistency (graphic standard deviation) of roughness, additional parameters (e.g., directionality and regularity of roughness) will be required to develop robust classification schemes. Well-controlled near-bottom sonar surveys supplemented with ground-truth observations and seafloor samples will provide the necessary information to establish statistically significant relationships between ultrahigh-resolution maps and the physical characteristics of the seafloor, and will be useful for understanding the processes of lava emplacement and crustal formation.

Acknowledgments

References

Arko, R., et al. (2007), The Global Multi-Resolution Topography (GMRT) synthesis, *Eos Trans. AGU*, *88*(52), Fall Meet. Suppl., Abstract IN51B-0405.

Baker, E. T., G. J. Massoth, K. Nakamura, R. W. Embley, C. E. J. de Ronde, and R. J. Arculus (2005), Hydrothermal activity on near-arc sections of back-arc ridges: Results from the Mariana Trough and Lau Basin, *Geochem. Geophys. Geosyst.*, *6*(9), Q09001, doi:10.1029/2005GC000948.

Baker, E. T., J. A. Resing, S. L. Walker, F. Martinez, B. Taylor, and K. Nakamura (2006), Abundant hydrothermal venting along melt-rich and melt-free ridge segments in the Lau back-arc basin, *Geophys. Res. Lett.*, *33*, L07308, doi:10.1029/2005GL025283.

Ballard, R. D., et al. (2000), The discovery of ancient history in the deep sea using advanced deep submergence technology, *Deep Sea Res., Part I*, *47*(9), 1591–1620, doi:10.1016/S0967-0637(99)00117-X.

Bezos, A., C. Langmuir, S. Escrig, P. Asimow, and S. Woods (2005), Mantle petrogenesis of the Eastern Lau Spreading Center basalts and andesites and the role of subduction-related fluids, *Eos Trans. AGU*, *86*(52), Fall Meet. Suppl., Abstract V41C-1469.

Carbotte, S. M., et al. (2004), New integrated data management system for Ridge2000 and MARGINS research, *Eos Trans. AGU*, *85*(51), 553, doi:10.1029/2004EO510002.

Carbotte, S. M., R. S. Detrick, A. Harding, J. P. Canales, J. Babcock, G. Kent, E. Van Ark, M. Nedimovic, and J. Diebold (2006), Rift topography linked to magmatism at the intermediate spreading Juan de Fuca Ridge, *Geology*, *34*, 209–212, doi:10.1130/G21969.1.

Caress, D. W., H. J. Thomas, W. J. Kirkwood, and P. G. Brewer (2006), An autonomous multibeam, sidescan, and subbottom survey of a methane hydrate outcrop in Barkley Canyon, offshore Vancouver Island, *Eos Trans. AGU*, *87*(52), Fall Meet. Suppl., Abstract MR43A-1063.

Chadwick, W. W., Jr., D. S. Scheirer, R. W. Embley, and H. P. Johnson (2001), High-resolution bathymetric surveys using scanning sonars: Lava flow morphology, hydrothermal vent and geologic structure at recent eruption sites on the Juan de Fuca Ridge, *J. Geophys. Res.*, *106*, 16,075–16,100, doi:10.1029/2001JB000297.

Cochran, J. R., D. J. Fornari, B. J. Coakley, R. Herr, and M. A. Tivey (1999), Continuous near-bottom gravity measurements made with a BGM-3 gravimeter in DSV Alvin on the East Pacific Rise crest near 9°31′N and 9°50′N, *J. Geophys. Res.*, *104*(B5), 10,841–10,861, doi:10.1029/1999JB900049.

Escartin, J., S. A. Soule, D. J. Fornari, M. A. Tivey, H. Schouten, and M. R. Perfit (2007), Interplay between faults and lava flows in construction of the upper oceanic crust: The East Pacific Rise crest 9°25′–9°58′N, *Geochem. Geophys. Geosyst.*, *8*, Q06005, doi:10.1029/2006GC001399.

Ferrini, V. L., D. J. Fornari, T. M. Shank, J. C. Kinsey, M. A. Tivey, S. A. Soule, S. M. Carbotte, L. L. Whitcomb, D. Yoerger, and J. Howland (2007), Submeter bathymetric mapping of volcanic and hydrothermal features on the East Pacific Rise crest at 9°50′N, *Geochem. Geophys. Geosyst.*, *8*, Q01006, doi:10.1029/2006GC001333.

Folk, R. L., and W. C. Ward (1957), Brazos River bar: A study in the significance of grain size parameters, *J. Sediment. Petrol.*, *27*, 3–26.

Fornari, D. J., and the WHOI TowCam Group (2003), A new deep-sea towed digital camera and multi-rock coring system, *Eos Trans. AGU*, *84*(8), 69, doi:10.1029/2003EO080001.

Fouquet, Y., et al. (1991), Hydrothermal activity and metallogenesis in the Lau back-arc basin, *Nature*, *349*, 778–781, doi:10.1038/349778a0.

Fouquet, Y., U. von Stackelberg, J. L. Charlou, J. Erzinger, P. M. Herzig, R. Muehe, and M. Wiedicke (1993), Metallogenesis in back-arc environments: The Lau Basin example, in *A Special Issue on Sea-Floor Hydrothermal Mineralization: New Perspectives*, *Econ. Geol.*, *88* (8), 2150–2177.

Fretzdorff, S., U. Schwarz-Schampera, H. L. Gibson, C.-D. Garbe-Schönberg, F. Hauff, and P. Stoffers (2006), Hydrothermal activity and magma genesis along a propagating back-arc basin: Valu Fa Ridge (southern Lau Basin), *J. Geophys. Res.*, *111*, B08205, doi:10.1029/2005JB003967.

German, C. R., D. P. Connelly, R. D. Prien, D. R. Yoerger, M. Jakuba, A. M. Bradley, T. Shank, K. Nakamura, C. H. Langmuir, and L. M. Parsons (2005), New techniques for hydrothermal plume investigation by AUV, *Geophys. Res. Abstr.*, *7*, Abstract EGU05-A-04361.

Ishibashi, J., J. E. Lupton, T. Yamaguchi, J. Querellou, T. Nunoura, and K. Takai (2006), Expedition reveals changes in Lau Basin hydrothermal system, *Eos Trans. AGU*, *87*(2), 13, doi:10.1029/2006EO020001.

Jacobs, A. M., A. J. Harding, G. M. Kent, and D. Kilb (2006), Multi-channel seismic reflection data and visualizations of combined datasets, in *Ridge 2000 Workshop Report: Lau Integrated Studies Site Focus Workshop*, pp. 7–8, Ridge 2000, La Jolla, Calif.

Jacobs, A. M., A. J. Harding, and G. M. Kent (2007), Axial crustal structure of the Lau back-arc basin from velocity modeling of multichannel seismic data, *Earth Planet. Sci. Lett.*, *259*(3–4), 239–255, doi:10.1016/j.epsl.2007.04.021.

Jakuba, M., D. R. Yoerger, A. Bradley, C. German, C. Langmuir, and T. Shank (2005), Multiscale, multimodal AUV surveys for hydrothermal vent localization, paper presented at Fourteenth International Symposium on Unmanned Untethered Submersible Technology (UUST05), Auton. Undersea Syst. Inst., Durham, N. H.

Jenness, J. (2003), Grid surface areas: Surface area and ratios from elevation grids, ArcView Extensions, electronic manual, Jenness Enterprises, Flagstaff, Ariz. (Available at http://www.jennessent.com/arcview/arcview_extensions.htm)

Jenness, J. S. (2004), Calculating landscape surface area from digital elevation models, *Wildlife Soc. Bull.*, *32*(3), 829–839, doi:10.2193/0091-7648(2004)032[0829:CLSAFD]2.0.CO;2.

Kinsey, J. C., L. L. Whitcomb, D. R. Yoerger, J. C. Howland, V. L. Ferrini, and O. Hegrenas (2006), New navigation post-processing tools for oceanographic submersibles, *Eos Trans. AGU*, *87*(52), Fall Meet. Suppl., Abstract OS33A-1678.

Kurras, G. J., M. H. Edwards, and D. J. Fornari (1998), High-resolution bathymetry of the East Pacific Rise axial summit trough 9°49′–51′N: A compilation of Alvin scanning sonar and altimetry data from 1991–1995, *Geophys. Res. Lett.*, *25*(8), 1209–1212.

Lundblad, E. R., D. J. Wright, J. Miller, E. M. Larkin, R. Rinehart, D. F. Naar, B. T. Donahue, S. M. Anderson, and T. Battista (2006), A benthic terrain classification scheme for American Samoa, *Mar. Geod.*, *29*(2), 89–111, doi:10.1080/01490410600738021.

Macdonald, K. C., J.-C. Sempere, and P. J. Fox (1984), East Pacific Rise from Siqueiros to Orozco fracture zones: Along-strike continuity of axial neovolcanic zone and structure and evolution of overlapping spreading centers, *J. Geophys. Res.*, *89*, 6049–6069, doi:10.1029/JB089iB07p06049.

Macdonald, K. C., et al. (1992), The East Pacific Rise and its flanks 8°–18°N: History of segmentation, propagation and spreading direction based on SeaMARC II and SeaBeam studies, *Mar. Geophys. Res.*, *14*, 299–344, doi:10.1007/BF01203621.

Martinez, F., B. Taylor, E. T. Baker, J. A. Resing, and S. L. Walker (2006), Opposing trends in crustal thickness and spreading rate along the back-arc Eastern Lau Spreading Center: Implications for controls on ridge morphology, faulting, and hydrothermal activity, *Earth Planet. Sci. Lett.*, *245*(3–4), 655–672, doi:10.1016/j.epsl.2006.03.049.

Pearce, J. A., M. Ernewein, S. H. Bloomer, L. M. Parson, B. J. Murton, and L. E. Johnson (1995), Geochemistry of Lau Basin volcanic rocks: Influence of ridge segmentation and arc proximity, in *Volcanism Associated With Extension at Consuming Plate Margins*, edited by J. L. Smellie, *Geol. Soc. Spec. Publ.*, *81*, 53–75.

Proskurowski, G., J. S. Seewald, E. Reeves, T. M. McCollom, J. Lupton, S. Sylva, and M. K. Tivey (2007), Volatile chemistry at Lau Basin hydrothermal sites: Basin-wide trends of slab carbonate influence and suggestions of abiotic methane oxidation at the Mariner vent site, *Eos Trans. AGU*, *88*(52), Fall Meet. Suppl., Abstract V34B-04.

Ridge 2000 (2006), *Ridge 2000 Workshop Report: Lau Integrated Studies Site Focus Workshop*, 19 pp., La Jolla, Calif. (Available at http://www.ridge2000.org/science/downloads/meetings/LauISSReport2006.pdf)

Roman, C. (2005), Self consistent bathymetric mapping from robotic vehicles in the deep ocean, Ph.D. dissertation, 129 pp., Mass. Inst. of Technol., Cambridge.

Roman, C., and H. Singh (2007), A self-consistent bathymetric mapping algorithm, *J. Field Robot.*, *24*, 26–51, doi:10.1002/rob.20164.

Scheirer, D. S., D. J. Fornari, S. E. Humphris, and S. Lerner (2000), High-resolution seafloor mapping using the DSL-120 sonar system: Quantitative assessment of sidescan and phase-bathymetry data from the Lucky Strike Segment of the Mid-Atlantic Ridge, *Mar. Geophys. Res.*, *21*, 121–142, doi:10.1023/A:1004701429848.

Schouten, H., M. Tivey, D. Fornari, D. Yoerger, A. Bradley, P. Johnson, M. Edwards, and T. Kurokawa (2002), Lava transport and accumulation processes on EPR 9 27′N to 10N: Interpretations based on recent near-bottom sonar imaging and seafloor observations using ABE, Alvin and a new digital deep sea camera, *Eos Trans. AGU*, *83*(47), Fall Meet. Suppl., Abstract T11C-1262.

Seewald, J., T. McCollom, G. Proskurowski, E. Reeves, M. Mottl, J. Sharkey, C. G. Wheat, and M. Tivey (2005), Aqueous volatiles in Lau Basin hydrothermal fluids, *Eos Trans. AGU*, *86*(52), Fall Meet. Suppl., Abstract T31A-0478.

Shank, T. M., et al. (2003), Deep submergence synergy: *Alvin* and ABE explore the Galapagos Rift at 86°W, *Eos Trans. AGU*, *84*(41), 425, doi:10.1029/2003EO410001.

Singh, H., L. Whitcomb, D. Yoerger, and O. Pizarro (2000), Microbathymetric mapping from underwater vehicles in the deep ocean, *Comput. Vision Image Understand.*, *79*(1), 143.

Soule, S. A., D. J. Fornari, M. R. Perfit, M. A. Tivey, W. I. Ridley, and H. Schouten (2005), Channelized lava flows at the East Pacific Rise crest 9°–10°N: The importance of offaxis lava transport in developing the architecture of young oceanic crust, *Geochem. Geophys. Geosyst.*, *6*, Q08005, doi:10.1029/2005GC000912.

Stout, K. (2000), *Three-Dimensional Surface Topography*, 2nd ed., 285 pp., Penton, London.

Tivey, M. K., P. Craddock, J. Seewald, V. Ferrini, S. Kim, M. Mottl, A. Sterling, A.-L. Reysenbach, C. G. Wheat, and the TUIM05MV Scientific Party (2005), Characterization of six vent fields within the Lau Basin, *Eos Trans. AGU*, *86*(52), Fall Meet. Suppl., Abstract T31A-0477.

Whitcomb, L. L., D. R. Yoerger, H. Singh, and J. Howland (2000), Advances in underwater robot vehicles for deep ocean exploration: Navigation, control, and survey operations, in *Robotics Research: The Ninth International Symposium*, pp. 439–448, Springer, New York.

White, S. M., R. M. Haymon, D. J. Fornari, M. R. Perfit, and K. C. Macdonald (2002), Correlation between volcanic and tectonic segmentation of fast-spreading ridges: Evidence from volcanic structures and lava flow morphology on the East Pacific Rise at 9°–10°N, *J. Geophys. Res.*, *107*(B8), 2173, doi:10.1029/2001JB000571.

White, S. M., R. Haymon, and S. M. Carbotte (2006), A new view of ridge segmentation and near-axis volcanism at the East Pacific Rise, 8°–12°N, from EM300 multibeam bathymetry, *Geochem. Geophys. Geosyst.*, *7*, Q12O05, doi:10.1029/2006GC001407.

Yoerger, D., A. Bradley, R. Bachmayer, R. Catanach, A. Duester, S. Liberatore, H. Singh, B. Walden, and M. A. Tivey (1996), Near-bottom magnetic surveys of the Coaxial Ridge segment using the Autonomous Benthic Explorer survey vehicle, *RIDGE Events*, *7*, 5–9.

Yoerger, D. R., M. Jakuba, A. M. Bradley, and B. Bingham (2007), Techniques for deep sea near bottom survey using an autonomous underwater vehicle, *Int. J. Robot. Res.*, *26*(1), 41–54, doi:10.1177/0278364907073773.

Zellmer, K. E., and B. Taylor (2001), A three-plate kinematic model for Lau Basin opening, *Geochem. Geophys. Geosyst.*, *2*(5), 1020, doi:10.1029/2000GC000106.